36

Practical Confocal Microscopy

Alan R. Hibbs, Glen MacDonald, and Karl Garsha

THE ART OF IMAGING BY CONFOCAL MICROSCOPY

This chapter is aimed at giving a practical overview of using confocal microscopes and monitoring their performance. Confocal microscopy is a multi-skilled endeavor that requires a considerable level of competence in sample preparation, knowledge of potential sources of artifact and appropriate controls samples, instrumentation evaluation and operation, computational post-processing, as well as knowledge of a multitude of fluorescent probes (Hibbs, 2004).

Do not overlook the specimen itself as a component of the imaging process. As living cells are often particularly optically active, it is important to understand the mechanisms of intentional as well as unintentional contrast generation in confocal microscopy. Appropriate controls are crucial to the production of reliable multi-dimensional image data.

Balancing Multiple Parameters

The goal of instrument adjustment during image collection on a confocal microscope is to balance a number of potentially conflicting parameters on the instrument. The main paradox involves achieving adequate spatial resolution while keeping cells alive and healthy or at least unbleached. Recording dynamic cellular processes with minimal light exposure may require a significant compromise in the degree of resolution that can be obtained.

Every image should be acquired using parameters that maximize its information content within the limitations of the selected mode of microscopy. Post-acquisition processing, such as deconvolution or three-dimensional (3D) Gaussian filtering, histogram stretching, or projections of multiple planes, can be employed to reveal the important details under photon-limited conditions (see Chapters 32 and 48, *this volume*).

MONITORING INSTRUMENT PERFORMANCE

The ability to determine relative dye concentrations, colocalization, Förster resonance energy transfer (FRET), shifts in emission spectra, and identity of ambiguous fluorescent signals is highly dependent on the accuracy and precision of a multitude of instrument functions. To ensure consistent peak performance, one must monitor performance at regular intervals and keep good documentation. Benchmarks of functionality can be organized around four major subsystems common to scanning microscopes: (1) illumination source, (2) signal detection subsystem, (3) scan raster mechanisms, and (4) lenses and other optical elements. In order for accurate and precise data to be recorded, not only must each subsystem perform well on its own merits, but they must also be carefully orchestrated to work together in synergy.

Illumination Source

Power Measurement

Obtaining consistent results from a confocal microscope requires knowledge of the actual laser power level at the specimen and its temporal stability. A well-equipped microscopy facility needs a reliable, accurate power meter (a photometer) suitable for making measurements at the specimen plane. Otherwise, low signal level can be wrongly attributed to poor specimen preparation or problems in the detection channel when the actual fault is low excitation power. Such devices may be acquired from optics companies such as Newport (Irvine, CA), Melles Griot (Carlsbad, CA), and Linos Photonics (Milford, MA), among others. Adjustments such as the re-alignment of the fiber to the laser output may occasionally be needed. Changes in the illumination stability often reflect the gradual deterioration of lasers and arc bulbs over the long term. As a laser cavity nears the end of its lifetime, it may also display a reduced output level that may be abrupt and very obvious. In lasers with multiple lines, it is common for one line to lose power before the others.

Tracking long-term changes in power output requires the use of standardized settings.[1] The appropriate dichroic mirror should be used for each laser line. Because objectives vary in terms of their transmission and pupil diameter, it is important to use the same objective for standard laser power measurements. To measure laser power, use the beam-parking or point-bleaching features to place a diffraction-limited point near the center of the field of view, and turn on the beam for an exposure of ~30 s. As the laser

[1] On instruments where the beam expander is under software control, the control should be disabled or it should be removed from the optical path.

Alan R. Hibbs • BIOCON, Melbourne, Australia
Glen MacDonald • Core for Communication Research, Virginia Merrill Bloedel Hearing Research Center, University of Washington, Seattle, WA, USA
Karl Garsha • Imaging Technology Group, Beckman Institute for Advanced Science and Technology, University of Illinois at Urbana-Champaign, IL 61801, USA

power is not modulated during beam-parking it is ideal for power measurement. On older scanners that do not have acousto-optic tuning filter (AOTF) beam blanking during retrace, use the maximum zoom setting.

The AOTF settings (or neutral density filters) should be configured to provide maximum power, and if there is a coarse adjustment for the laser power, this should be maximized as well. The power meter sensor should be carefully positioned over the field of view near the focal plane of a dry objective and perpendicular to the optical axis. Because most sensors are not equally sensitive across the entire surface, use a stable sensor mounting system so as to use the same area of the sensor surface. Be sure the laser power meter is set to the appropriate detection wavelength.[2]

To measure the power, start the point bleach sequence for a single laser line and record the meter readout. Repeat for each laser line in turn. For accurate readings the room should be dark, the lasers adequately warmed up, and several measurements should be taken to check data precision.

Similar readings taken in the standard scanning mode will be lower than this value if the laser beam is blanked by the AOTF during the flyback and during the interval between consecutive frames.

Laser Stability

Although laser stability on the order of seconds can be measured with a photometer, rapid oscillations of laser output are beyond the temporal resolution of the power meter. To measure high frequency stability, image a bright standardized, stable fluorescent sample such as a coverslipped piece of fluorescent plastic (Chroma Technologies Inc., Rockingham, VT; Applied Precision, Issaquah, WA), or a high concentration of fluorescent dye in oil (fluorescent seas; see Chapters 2 and 35, *this volume*; also Model and Burkhardt, 2001). To reduce photobleaching, use a freshly prepared, standardized dilution of fluorochrome in an index-matched solvent.[3]

On inverted microscopes, use chambered coverslips with multiple wells (Nalge Nunc International, Rochester, NY) to hold the fluorescent liquid. Carefully prepared concavity slides (Electron Microscopy Sciences, Hatfield, PA) can be used as an alternative on upright microscopes. It is a good idea to centrifuge the test solution in order to remove particulates prior to use. Focus the microscope into the bulk fluorescent standard near (but not at) the dye–coverslip interface.

Set up a two-dimensional (2D) time series with an appropriate acquisition interval and overall duration. The scan area can be reduced to only a few lines in order to reduce the acquisition interval for greater temporal resolution. Settings should be configured such that the laser power is standardized to a value high enough to provide a reasonably noise-free image, yet low enough that bleaching is not a problem, and the detectors adjusted such that the measured mean pixel intensity is within the linear response range (see Chapter 2, *this volume*). Analyze the acquired dataset by eye for obvious indications of instability, such as some lines being brighter than others, etc., or by graphing the mean intensity of each time point. Small, periodic variations will be made more obvious in a Fourier transform of the data.

Scan Raster and Focus Positioning

Spatial measurements and accurate morphometric classification rely on the accuracy and precision of the mechanisms used to move the focal volume through the specimen in the *x*-, *y*-, and *z*-dimensions. **From a practical standpoint, measures of the lateral and axial resolution on a laser-scanning instrument are meaningless unless the accuracy and precision of pixel-to-pixel spacing in the *x*, *y*, and *z* can be verified.** A non-uniform scan speed will also result in differential exposure of localized areas within the field of view (Carlsson, 1991). This confounds accurate photometry and can result in increased phototoxicity when living specimens are being imaged (Fig. 36.1).

x and *y* Galvanometers

Standards for verifying lateral scan accuracy are easily purchased or fashioned from readily available components. Because the response of the galvanometer to a change in either zoom or scan speed frequently departs from an ideal linear relationship, it is not adequate to confirm scan calibrations at a single magnification and horizontal scan frequency, and, thus, one needs a standard specimen that can be used at high as well as low zoom settings. A grid standard provides an efficient means of evaluating both *x*- and *y*-scan rasters simultaneously. Suitable standards include a 2000-mesh transmission electron microscope (TEM) grid mounted in appropriate media (Electron Microscopy Sciences, Hatfield, PA), an etched silicon 10 µm grid standard for reflected light microscopy (Electron Microscopy Sciences), a carbon replica of a diffraction

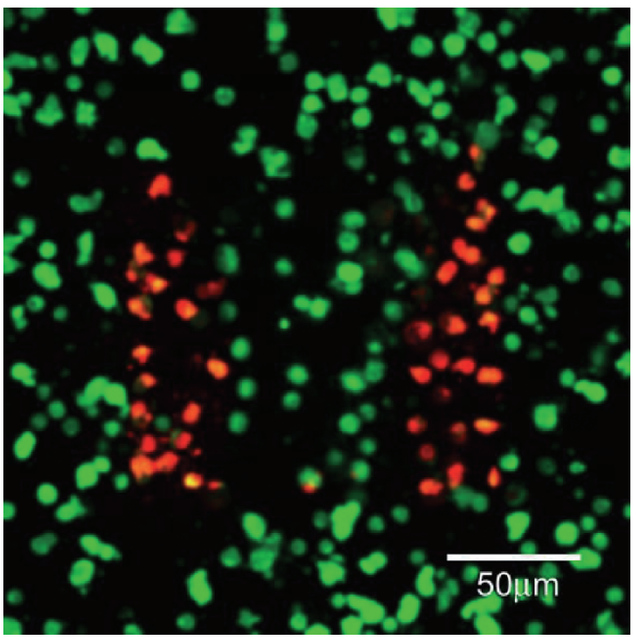

FIGURE 36.1. Differential phototoxicity as a result of uneven scan speed across the field of view. In this image, metabolically-active cells are stained with fluorescein diacetate (green); the onset of propidium iodide (red) indicates compromise of the plasma membrane associated with cell death. The speed of the scan raster was slower at the edges than in the center of the field of view in this case.

[2] Most meters actually measure the number of photons/second. As red photons carry less energy than blue ones, the meter needs to know the wavelength in order to calculate the energy/second or power.

[3] Bleaching can be removed as a variable by using a coverslipped, first-surface mirror as the test specimen. When viewed using reflected light, such a specimen produces a very high signal level (and consequently a very low level of Poisson noise), although system vibrations are more likely to account for any variations that you see due to the surface going in and out of focus, than by laser instability. This vibration sensitivity can be reduced by using an objective with low NA.

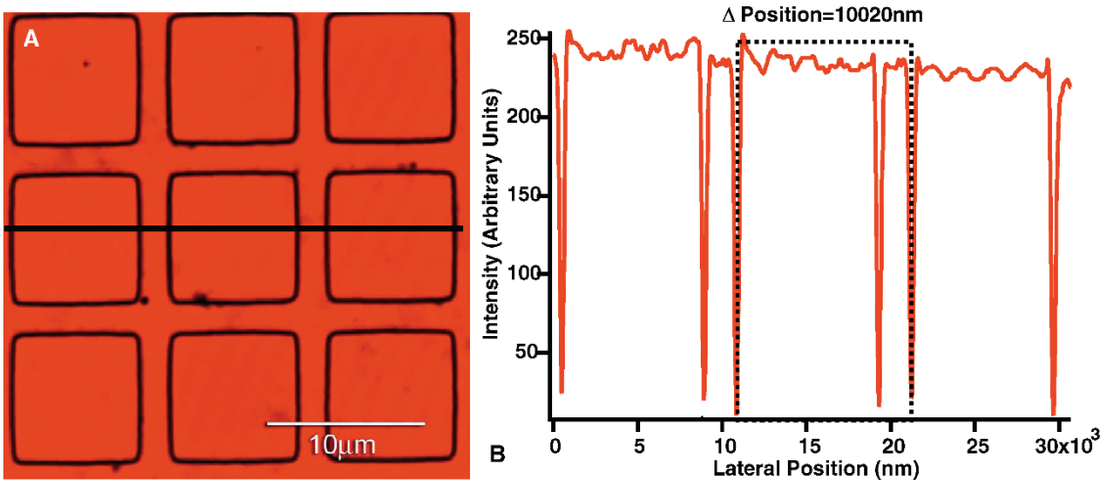

FIGURE 36.2. A well-calibrated system. (A) The standard in this case is a reflective etched silicon standard designed for reflected light microscopy. Each square is 10 microns per side; (B) a graph of intensity as a function of position on the black line in (A). Quantitative measurements confirm the accuracy and precision of the *x*- and *y*-galvanometers in this example.

grating or MBL-NNF Test Slide[4] (see Chapter 35, *this volume*), and related products such as the Microscopic Image Analysis Micrometer (Edmunds Optics, Barrington, NJ) and the Richardson test slide (Electron Microscopy Sciences). If a TEM grid (or other uncharacterized standard) is used, the accuracy and precision of center-to-center spacing between grid bars can be accurately determined using a properly calibrated widefield system.

Measurements of the center-to-center (side of one grid bar to the same side of the next) distance at different points within the field of view should be conducted for both *x*- and *y*-axes in conventional *xyz*-imaging mode. It is important to realize the effect that under-sampling can have on such measurements; sampling intervals for the scan resolution should satisfy the Nyquist criteria (see Chapters 2, 4, and 35, *this volume*). A well-calibrated instrument will have accuracy within 1% of the known value and less than 1% variability between measurements. This should hold at both high and low zoom values, and across all scan speeds. Results from an instrument that is well calibrated can be seen in Figure 36.2, and the opposite is shown in Figure 36.3.

z-Drive Mechanism

The performance of the *z*-stepping or *z*-scanning system can be evaluated using large diameter beads, for example, 10.2 µm (see Table 36.1), carefully mounted in an **index-matched** [i.e., refractive index (RI) = 1.515; see Chapters 8 and 20, *this volume*] semi-solid or high-viscosity mountant. High axial resolution requires proper refractive index with a high numerical aperture (NA) oil-immersion objective (designed for RI of 1.51; polystyrene beads have RI between 1.55 and 1.59). Do not use a dry objective (Carlsson, 1991).

Commercially prepared fluorescent bead calibration slides can be purchased from Spherotech and Molecular Probes (Table 36.1). *z*-Calibration measurements should be performed at both high and low magnification by making *xz*-images across the center of a bead. The height of several beads from several levels within the *z*-plane should be measured. The diameter of the bead with respect to *z* is taken as the distance between half-maximum intensity values on the steep-sloped rising and falling intensity gradients that indicate the top and bottom of the bead. The accuracy and precision of the values obtained are then compared to the stated tolerances of the calibration beads. Unless the calibration beads have been severely compressed, the mean value and standard deviation taken from a sample should be the same in the *xz*-image as in the *xy*-image [Fig. 36.4(A,B)]. A large systematic departure from the values as measured with respect to the *xy*-plane likely represents poor performance of the *z*-movement mechanism, miscalibration of the control mechanisms, or the use of a mounting or immersion liquid having the wrong RI for the lens in use.

z-Positioning Stability

In both volumetric imaging and 2D time-lapse imaging, it is important that the relationship between the position of the sample and the optics is stable. As noted in the earlier footnote, this can be assayed using a mirror standard viewed in reflected light (described below under tests for axial resolution) over a time course. Motion of structures in an *xy*-image of the mirror surface shows vibration, while collecting a time-lapse series of 3D images through the reflective interface will reveal stage or focus drift. Rapid *xz*-scanning over time can assist in resolving high frequency drift. After acquisition, the position of the reflection intensity maximum with respect to *z* can be found at each time point and plotted as a function of time.

Vibration can be reduced by using a vibration-isolation table and making sure that all the wires or hoses connecting the table to the outside world are bent to reduce their ability to transmit mechanical forces. The most likely cause of drift is temperature change, often caused by the air conditioning going on and off, or in actual use, by components involved in heating the specimen and the objective for living-cell studies. The solution is to insulate your setup from changes in room air and run stage-heater controllers in the open-loop mode or place the entire microscope in a heated enclosure (see Chapter 19, *this volume*).

Optical Performance and Objective Lenses

Because the performance of the objective is crucial to the overall performance of an imaging system (see Chapter 11, *this volume*),

[4] Louie Kerr (Marine Biological Laboratory, Woods Hole, MA) has fabricated suitable test slides in the past using electron beam lithography at the National Nanofabrication Facility (NNF) at Cornell University. He expects to do so in the future.

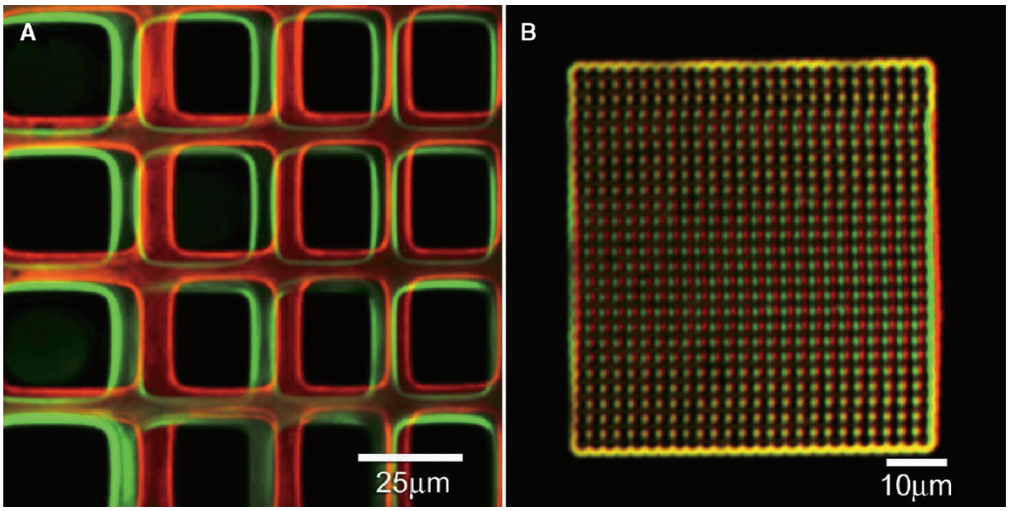

FIGURE 36.3. A malfunctioning system. (A) Observation at low magnification indicates problems with both accuracy and precision between scans. Two scans taken in sequence are indicated by the red and green channels of the image. (B) A scan taken at higher magnification on the same instrument. The standard in this case is milled into a coverslip surface with a focused ion beam (kind gift of Dr. Carlos Martinez, NIST, Gaithersburg, MD). Again, red and green components of the image reflect the lack of precision. Wavering in the scan raster appears as distortion in the grid standard. The square pattern appears rectangular (narrower in the *x*-direction) because of poor calibration of the *x*-scan galvanometer.

TABLE 36.1. Sources of Fluorescent Beads

Manufacturer	Address	Telephone	Web site/E-Mail
Bangs Laboratories, Inc.	9025 Technology Drive Fishers, IN 46038–2886 USA	Phone: +1 317-570-7020 USA: +1 800-387-0672 Fax: +1 317-570-7034	www.bangslabs.com info@bangslabs.com
Brookhaven Instruments, Ltd.	Chapel House, Stock Wood Redditch, Worcestershire B96 6ST, UK	Phone: +44 (0) 1386-792727 Fax: +44 (0) 1386-792720	www.brookhaven.co.uk enquiries@brookhaven.co.uk
Duke Scientific Corporation	2463 Faber Place Palo Alto, CA 94303 USA	Phone: +1 650-424-1177 USA: +1 800-334-3883 Fax: +1 650-424-1158	www.dukescientific.com info@dukescientific.com
G.Kisker GbR Produkte f.d.Biotechnologie	Postfach 1329 48543 Steinfurt Germany	Phone: +49 2551-864310 Fax: +49 2551-864312	www.kisker-biotech.com contact@kisker-biotech.com
Molecular Probes, Inc.	29851 Willow Creek Road Eugene, OR 97402 USA	Phone: +1 541-465-8300 Fax: +1 541-335-0504 Order: + 1 800-438-2209	www.probes.invitrogen.com order@probes.com
Polysciences, Inc.	400 Valley Road Warrington, PA 18976 USA	Phone: +1 215-343-6484 USA: +1 800-523-2575 Fax: +1 800-343-3291	www.polysciences.com info@polysciences.com
Sigma-Aldrich Corp.	3050 Spruce Street St. Louis, MO 63103 USA	Phone: +1 314-771-5765 USA: +1 800-325-3010 Fax: +1 314-771-5757	www.sigmaaldrich.com OC_DOM_HC@sial.com
Spherotech, Inc.	1840 Industrial Dr. Suite 270 Libertyville, IL 60048-9467 USA	Phone: +1 847-680-8922 USA: +1 800-368-0822 Fax: +1 847-680-8927	service@spherotec.com jwsphero@aol.com

These vendors offer beads down to subresolution sizes in single and multiple wavelengths. Many offer larger beads in a variety of configurations. Larger beads may be solidly fluorescent, contain surface rings, overlapping concentric rings, concentric rings that do not overlap, and combinations of solid and ring labels. Some vendors in this list also offer silica, glass, or melamine beads that possess different physical properties compared to the commonly used polystyrene or latex.
This list does not include vendors of fluorescent beads where the bead preparations are specifically designed for flow cytometry.

all objectives should be tested for performance. Objectives do vary within brand and type and should be carefully compared before purchase and then regularly monitored (see Chapter 11, *this volume*, for more details). The most common tests of imaging optics, those for lateral and axial resolution and chromatic aberration, should be performed periodically as objective lens performance may deteriorate over time.

Spherical aberration created by the specimen is a serious constraint in the creation of high-quality images, particularly when imaging living biological material. As described in detail in Chapters 2, 7, and 20, when using an oil-immersion lens to image living biological material there will be a serious mismatch in RI between the design parameters of the objective and the aqueous sample. Even using an oil-immersion objective with a sample mounted in a media with a relatively high RI, such as glycerol (RI = 1.47), there is still be a significant level of spherical aberration present.

The best plan is to use objective lenses designed for the imaging conditions under which they are being used. Some objectives are equipped with a collar to correct for routine variations in coverslip thickness, as noted in Table 36.2. However, RI mismatches can also be partially corrected by coverslip-thickness correction collars or using the automated spherical-aberration corrector (SAC) now offered by Intelligent Imaging (Denver, CO). This will greatly diminish spherical aberration, and result in improved resolution and signal level, particularly when imaging deep into the sample. The effect of spherical aberration on signal intensity is readily demonstrated by collecting an *xz*-image into a dilute fluorescent solution such as 0.01% coumarin in water (Fig. 36.5). In Figure 36.5(A,B), a 40× NA 0.60 non-immersion dry objective lens has been used to image into a dilute coumarin solution contained in a sealed imaging chamber. The base of the chamber is a 0.17 mm thick coverslip, with the correction collar on the objective set for 0.17 mm [Fig. 36.5(A)] or 0.5 mm [Fig. 36.5(B)]. Even when the spherical aberration collar is correctly matched to the thickness of the coverslip, the intensity profile diminishes significantly as the focus plane moves away from the coverslip [Fig. 36.5(A)]. This drop-off in intensity is due to the RI mismatch between the immersion media (in this case, air) and the sample (water). If the spherical aberration correction collar is adjusted to 0.50 mm, while retaining a coverslip thickness of 0.17 mm, then the zone of maximum intensity in the image is moved farther into the sample [Fig. 36.5(A)]. This simple adjustment can be used to collect good images over a limited range of depths within living tissue samples using a non-immersion air lens.

Figure 36.5(C) shows the performance of a 40× NA 1.20 water-immersion lens (with 0.17 mm coverslip correction). Because the objective is used with water on both sides of the coverslip, the total thickness of water and glass between the front of the objective and the focus plane does not change with focus position and therefore, intensity of the signal in this *xz*-image does not diminish throughout the full depth of the scan (200 µm).

TABLE 36.2. Coverslip Thickness and Refractive Index

Designated Size	Tolerance (mm)
#00	0.06–0.08
#0	0.08–0.12
#1	0.13–0.16
#1.5	0.16–0.19
#2	0.19–0.23
#3	0.28–0.30
#4	0.38–0.42
#5	0.50–0.60
Refractive Index at 20°C for Commonly Used Glass	
Desag D-263	(546 nm) = 1.5255
	(588 nm) = 1.5230
Corning 0211	(589 nm) = 1.5230

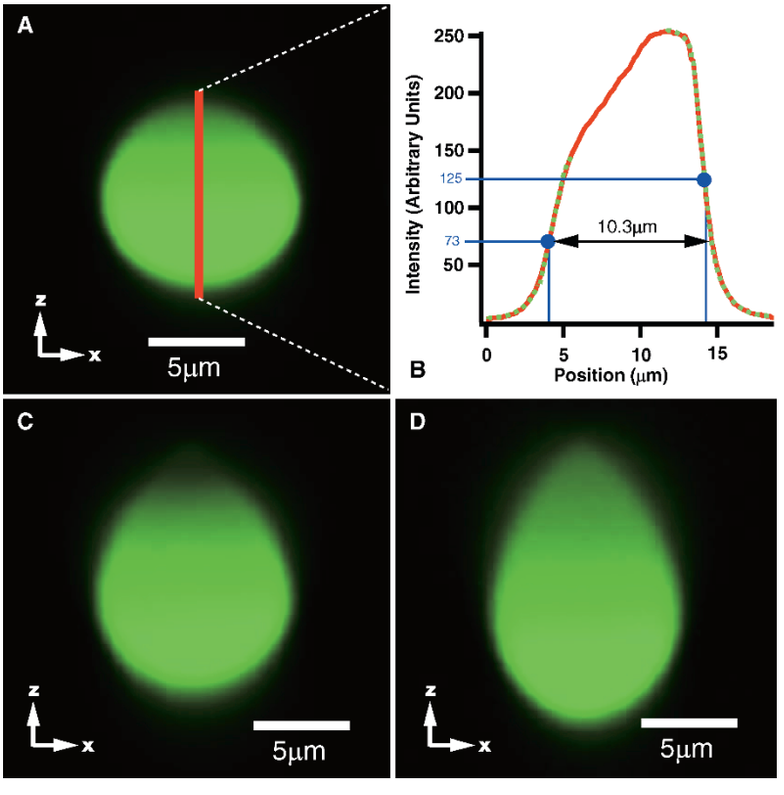

FIGURE 36.4. Checking *z*-positioning calibration using fluorescent beads. (A) 10.2 µm polystyrene spheres in immersion oil. The data maintain the correct aspect ratio, and accurate measurements in the *z*-axis are possible with an oil-immersion lens. (B) Measurement of calibration beads in the *z*-axis under properly index-matched conditions permits evaluation of the *z*-drive calibration. The midpoint on each of the steep-sloped lines depicting the edge response of the top and bottom limits of the bead are found (*green/red dotted lines*). The distance between these points on the *x*-axis of the intensity plot is the height of the bead. Note that the intensity of the bead is not constant through the diameter of the bead due to absorption of excitation light by the bead. For this reason, the halfway points of the bottom and top edge response are located at different intensity levels. In this case the *z*-drive (a *z*-galvanometer stage) is performing well, and measurement of the axial dimensions of the calibration beads are both accurate and precise. (C) The same beads in a classic 9:1 glycerol/PBS buffer mountant of RI = 1.43 viewed with an oil-immersion lens. Significant distortion in the *z*-axis is evident due to spherical aberration as well as self-lensing. Accurate measurements with respect to *z* are not possible under these conditions. (D) 10.2 micron polystyrene spheres in water (RI = 1.32) viewed with an oil-immersion lens. Distortion in the *z*-axis is exacerbated in accordance with Snell's law.

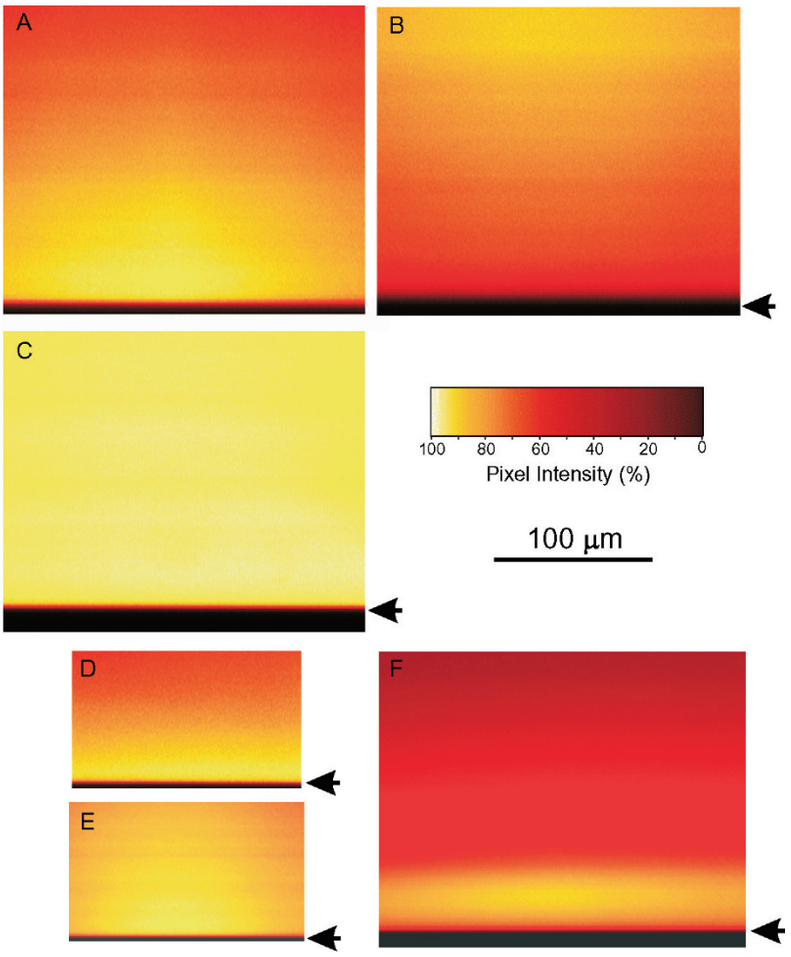

FIGURE 36.5. Correcting for spherical aberration. *xz*-images were collected on a Zeiss 510 META confocal microscope while imaging into (1) a dilute aqueous fluorescent coumarin solution (approximately 0.1 m*M*) and (2) green fluorescent plastic. The 488 nm blue laser line from an argon-ion laser was used for excitation, and the fluorescent light between 510 and 520 nm was collected into a single detection channel. Each image represents a single line collected at increasing depth (1 µm deeper per scan) within the solution or plastic. The position of the coverslip is marked with an arrow (←). All images were obtained using a 0.17 mm thick coverslip, with various adjustments of coverslip correction collars as described below. All images were collected using a pinhole size of 1 Airy disk. (1) Imaging into fluorescent aqueous media: a Zeiss LD-Achroplan 40× 0.60 NA dry lens was used to collect images into the fluorescent aqueous media with the coverslip thickness correction collar set to (A) 0.17 mm and (B) 0.50 mm. A Zeiss C-Apochromat 40 × 1.2 NA water-immersion lens with coverslip-correction collar set to 0.17 mm (C), and a Zeiss Plan-Apochromat 63 × 1.4 NA oil-immersion lens with 0.17 mm coverslip correction (D) were used to collect *xz*-images in the fluorescent coumarin solution. (2) Imaging into fluorescent plastic: a 0.17 mm thick coverslip was placed on the surface of a small sheet of green fluorescent plastic using a small amount of immersion oil between the coverslip and the plastic. *xz*-images were collected using a Zeiss Plan-Apochromat 63 × 1.4 NA oil-immersion lens with 0.17 mm coverslip correction (E) and a Zeiss C-Apochromat 40 × 1.2 NA water-immersion lens with the coverslip thickness correction collar set to 0.17 mm (F).

In Figure 36.5(D), a 63× NA 1.40 oil-immersion lens (corrected for 0.17 mm thick coverslip) has been used to image into the dilute coumarin solution. The severe RI mismatch between the immersion media (oil) and the sample (aqueous solution of coumarin) results in a significant reduction in the intensity of the fluorescent signal with increased imaging depth. The *z*-position of maximum signal detection is nearly always located close to the coverslip when using an oil lens to image into samples mounted in aqueous media. Oil-immersion lenses do not have spherical aberration correction collars.

Lateral Resolution

The lateral resolution of a digital microscope is usually measured with either a subresolution point source standard or a special test slide (see Chapter 35, *this volume*; Stark *et al.*, 2003).

Subresolution Beads

The 3D diffraction pattern characteristic of a microscopic imaging system is known as a point spread function (PSF; see Fig. 36.6; Chapters 7, 11, and 20, *this volume*; also Hiraoka *et al.*, 1990; Shaw and Rawlins, 1991; Wilson and Juškaitis, 1995; Scalettar *et al.*, 1996; Booth and Wilson, 2001; Wallace *et al.*, 2001; Cox and Sheppard, 2004). The PSF defines the spatial resolution of a particular optical train. Where deconvolution software is employed, one should record a library of PSF images for each objective lens and wavelength (see Chapter 11, *this volume*).

Fluorescent polystyrene beads measuring less than 200 nm (or even less than 100 nm) can be purchased prelabeled with dyes suitable for measuring resolution at different wavelengths (see Table 36.1 for a list of suppliers). They are conveniently prepared for imaging by allowing a few microliters of a bead suspension to spread over, and dry onto, the surface of a coverslip.[5] This ensures that all the beads are in the same focal plane and also eliminates Brownian motion. Most aqueous mounting agents used for fluorescent samples can be used with beads, but take care when using solvent-based mountants or immersion oil as the dyes may leach out or the beads may even dissolve.

The PSF is acquired by collecting a *z*-series extending about 6 to 8 µm axially above and below the bead. The pixel size and focus interval should be appropriate for the objective (i.e., 0.08 µm pixels and 0.3 µm focus step for NA 1.4, and 0.16 µm pixels and 1.2 µm focus step for NA 0.7).

Select single beads that are well separated from others and near the center of the field. Because Poisson noise imparts a great degree of ambiguity to such images, either select a slow scan speed or Kalman average at least three scans during image collection. Most deconvolution software packages capable of utilizing a measured PSF also have a provision for averaging several individual PSF volumes together to reduce from the effects of noise, drift, focusing errors, and intensity fluctuations in the illumination.

[5] The coverslip should be first cleaned by soaking in 1% HCl in 70% ethanol for 5 min, then rinsing thoroughly with H_2O and air drying. Application of the beads in 70% ethanol will aid in dispersion, although prolonged exposure may extract the dye.

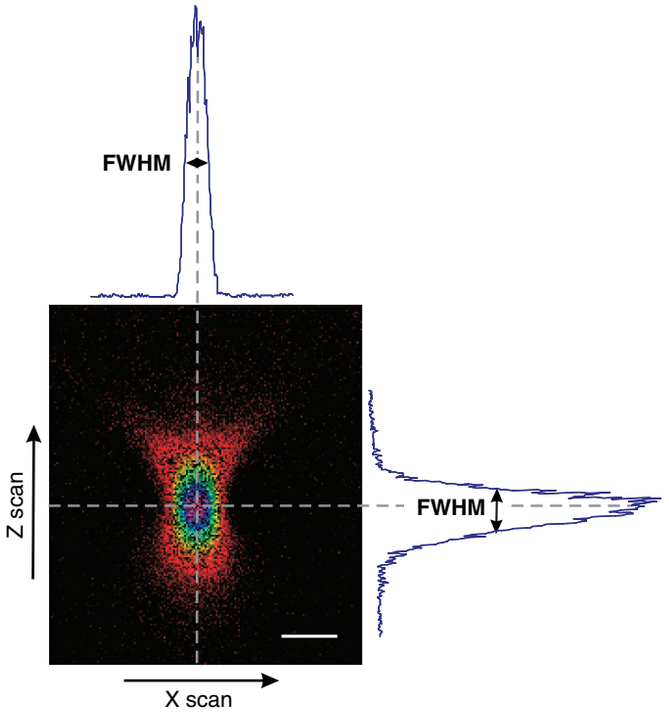

FIGURE 36.6. Determining *xy*- and *z*-resolution using fluorescent beads. The *x*-, *y*-, and *z*-resolution of a confocal microscope can be determined by imaging latex beads or quantum dots that are smaller than the resolution limit of the instrument. The beads will need to be immobilized by attaching them to the glass coverslip (e.g., by coating the coverslip with poly-L-lysine). The image shown here is a single *xz* optical slice taken through a small subresolution fluorescent latex bead (0.03 µm diameter) attached to a coverslip using poly-L-lysine and mounted in aqueous media. The image was collected on a Leica SP2 laser-scanning confocal microscope using a Leica 60 × 1.20 NA water-immersion objective. The FWHM, derived from the plot of the intensity profile in the *x*- and *z*-directions can be used to determine the resolution limit of the instrument. The scale bar represents 300 nm.

The lateral resolution of a PSF is taken as full width at half maximum (FWHM, the width of the intensity peak at 50% of its maximum intensity; see Fig. 36.6). The FWHM is measured by first finding half the maximum peak height of the intensity profile above background ($I_{\text{half max}}$, Eq. 1) and then determining the width of the intensity profile at $I_{\text{half max}}$ (denoted by the double ended arrow in Fig. 36.6).

$$I_{\text{half}} = \frac{I_{\text{max}} - I_{\text{background}}}{2} + I_{\text{background}} \qquad \textbf{(1)}$$

A projection along the *z*-axis and through the center of a volumetric dataset of a point source will ensure that the centroid of the intensity distribution is measured.

Some drawbacks to using fluorescent polystyrene spheres include the fact that they may bleach under high zoom or high laser intensity conditions and, after a time the dye may leach into organic mountants such as immersion oil.

Resolution Test Slides

As an alternative to point source standards, lateral resolution can be tested using specially designed microscopy standard slides such as the Richardson Test Slide Gen III (Richardson Technologies Inc., Toronto, Canada), the Microscopic Image Analysis Micrometer (Edmund Optics, Barrington, NJ), and the MBL-NNF Test Slide (Marine Biological Laboratory, Woods Hole, MA). The aforementioned slides have periodic line gratings of various spatial frequencies that are usually imaged in the reflected light mode, although some varieties are printed using fluorescent phosphors. The spatial frequency at which the image contrast disappears is taken as the resolution limit. This test emphasizes the relationship between contrast and resolution. This relationship is described by the **contrast transfer function** (CTF; see Chapters 1, 2, 4, and 8, *this volume*; also van der Voort *et al*., 1988; Pawley, 1994; van den Doel *et al*., 1998; Young, 2000).

Axial Resolution

Because *z*-resolution is affected by the setting of the adjustable pinhole (or pinholes as the case may be), as well as by the NA and wavelength, it is prudent to take measurements over the full range of pinhole settings (Fig. 36.7). Doing so will also reveal anomalies in the pinhole alignment. Misaligned pinholes will yield poor results for axial resolution and the expected relationship between pinhole diameter, signal intensity, and axial resolution will be disturbed (see Chapters 2, 3, 8, 11, and 22, *this volume*; also Cox and Sheppard, 2004).

Two methods are frequently employed to judge *z*-resolution. The first is the use of subresolution fluorescent particles to generate a PSF as above (Ho and Shao, 1991; Shaw and Rawlins, 1991). The second approach involves making an *xz* reflected light image of the surface of a mirror slide as described below (Ho and Shao, 1991; Visser *et al*., 1991; Cox, 1999; Zucker and Price, 2001a).

Axial Resolution Using a Mirror

A front-face mirror slide can be purchased (Electron Microscopy Sciences; Spherotech, Libertyville, IL) or made from a high-quality coverslip onto which a reflective metal surface has been deposited on one side using either sputter coating or vacuum depo-

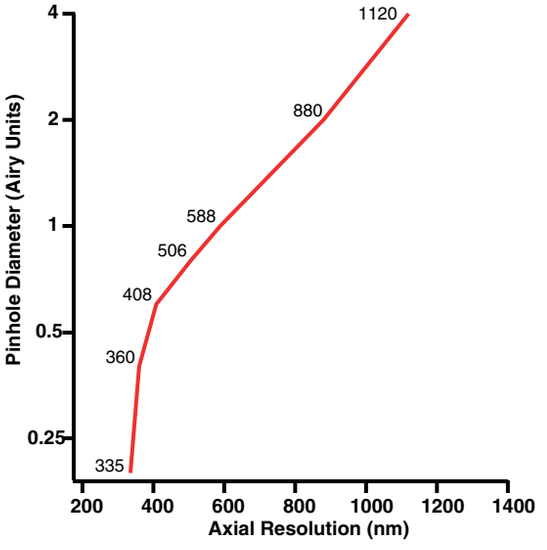

FIGURE 36.7. Axial resolution as a function of pinhole diameter. Measurements were conducted using a mirror standard with a 63× oil-immersion objective with NA 1.32.

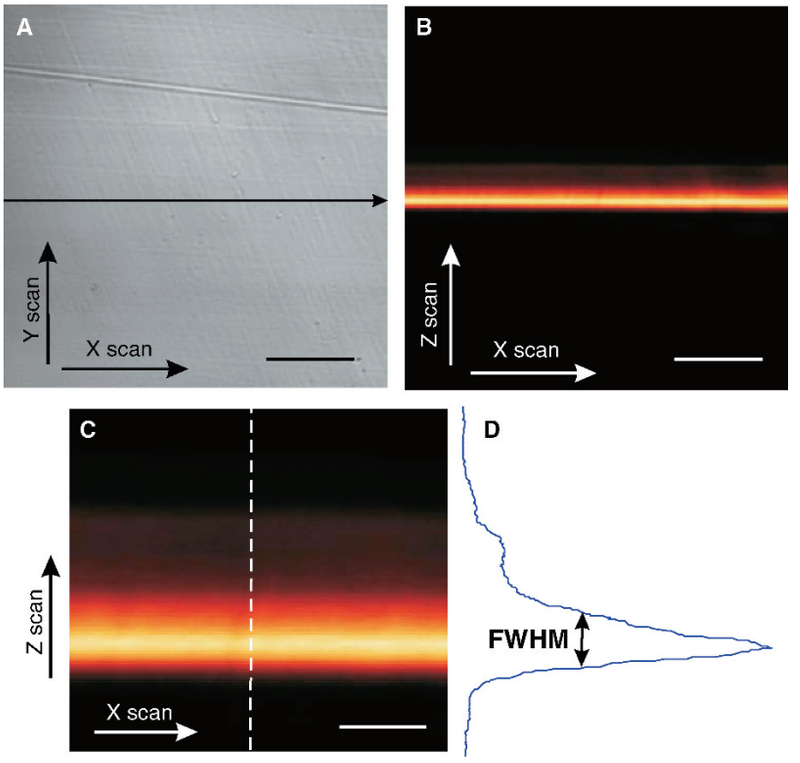

FIGURE 36.8. Determining *z*-resolution using a mirror. Backscatter images of a front surface silvered mirror using a Nikon 100× 1.40 NA oil-immersion lens on a Bio-Rad MRC-1024 confocal microscope with the 488 nm blue line from an argon-ion laser and a pinhole size of 1 Airy disk. The front-surfaced mirror was imaged by placing a small drop of immersion oil directly on the mirror surface and then placing a coverslip onto the oil. Immersion oil was then placed on top of the coverslip to create a continuum with the objective lens. (A) Backscatter image of the mirror surface (*xy*-image), (b) backscatter image through the mirror surface (*xz*-image), and (C) confocal zoom of a small section of the *xz*-image in (B) showing an intensity profile graph (D) at the position of the dotted line in image (C). The full-width at half-maximum (FWHM) of the intensity profile shown in (D) (measured in microns) is a measure of the *z*-resolution of the instrument. The slight asymmetry of the profile is due to a small amount of spherical aberration of the optical system. To establish whether this is due to an imperfection in the objective lens you would need to rigorously establish that the preparation of the sample has not introduced minor optical aberrations. The asymmetry of the plot shows the presence of spherical aberration. The scale bar in (A) and (B) represents 1.6 µm and in (C) represents 0.4 µm.

sition (Fig. 36.8). The coverslip should be mounted on the slide with the metallic side away from the objective. Purchased mirrors must be coverslipped (immersion oil makes a good mountant).

When determining axial resolution using a reflective surface, use a neutral density filter or the AOTF to reduce laser power to as low as possible (less than 100 µW should be adequate) and choose dichroic and filter settings that allow the wavelength of the laser line to reach the detector. Adjust the focus until you begin to detect a signal with the pinhole fully open. Then reduce the pinhole size as the reflection signal increases. At the focus position producing the highest reflected signal, adjust the PMT gain to create a bright image that does not quite saturate any pixels [Fig. 36.8(A)].

The mirror should then be moved to an area lacking major defects and an *xz*-image (vertical section) through the surface of the mirror is collected [Fig. 36.8(B)]. The upper and lower focus limits should be set sufficiently far apart to collect all the diffraction maxima. The *z*-step should be chosen to allow for more than Nyquist sampling through the profile of the mirror [Fig. 36.8(C)]. An *xz*-intensity profile through the mirror can also be obtained by collecting a stack of *xy*-images, and then extracting the *xz*-image using suitable software. The field curvature from any lens can be tested using either a mirror or a thin fluorescent film by collecting *xy*-scans or a *z*-series. Collect a 3D data stack that includes the full depth of the reflection image over the entire field at zoom = 1. An *xz*- or *yz*-profile through this stack will reveal the degree of curvature [Fig. 36.8(C); also see Chapter 11, *this volume*].

Asymmetry in the *xz*-profile through the mirror is usually indicative of spherical aberration. In the example shown in Figure 36.8, a slight asymmetry is evident. The use of incorrect immersion media or incorrect settings on the spherical aberration correction collar (often marked as a coverslip thickness or immersion media correction collar) will induce spherical aberration.

Chromatic Registration

For multi-channel laser scanning microscopy, it is important that the spatial registration of all channels can be confirmed. This is particularly true where experiments involve colocalization and/or ratiometric measurements. Probable sources of lateral chromatic registration error are found in situations where lasers delivered through separate fibers (or direct couplings) are used together, and/or when different optics such as dichroic beam-splitters or beam expanders are used for separate channels in an automated sequential-scanning strategy. Lens aberrations or mismatched optics can also be a source of lateral chromatic aberration (see Chapter 7, *this volume*). Although the laser launch into the scanhead is aligned when the instrument is installed, measurements should be conducted immediately following installation or just before the end of any service call. Widefield systems also suffer from alignment problems when filter cubes and dichroic mirrors are moved. In addition, the relay lenses in some camera couplers impart chromatic aberration.

Lateral Chromatic Registration

This aberration can cause points in the image to be shifted radially in a wavelength-dependent manner that becomes progressively larger towards the periphery of the field (see Chapter 7, *this volume*). The relatively large (4–15 µm in diameter) multi-labeled Focal Check beads marketed by Molecular Probes (Eugene, OR) are useful for evaluating the lateral registration of multiple channels. These beads are made of a series of fluorescent shells, each of which is excitable at a different wavelength. A multi-channel image through the lateral central plane of these spheres shows a different colored ring for each channel. An overlay of all channels should depict colocalized signals (Fig. 36.9).

Alternatively, one can use a mixture of subresolution beads (Zucker and Price, 2001a) that fluoresce over a wide range of wavelengths providing that individual channels are excited

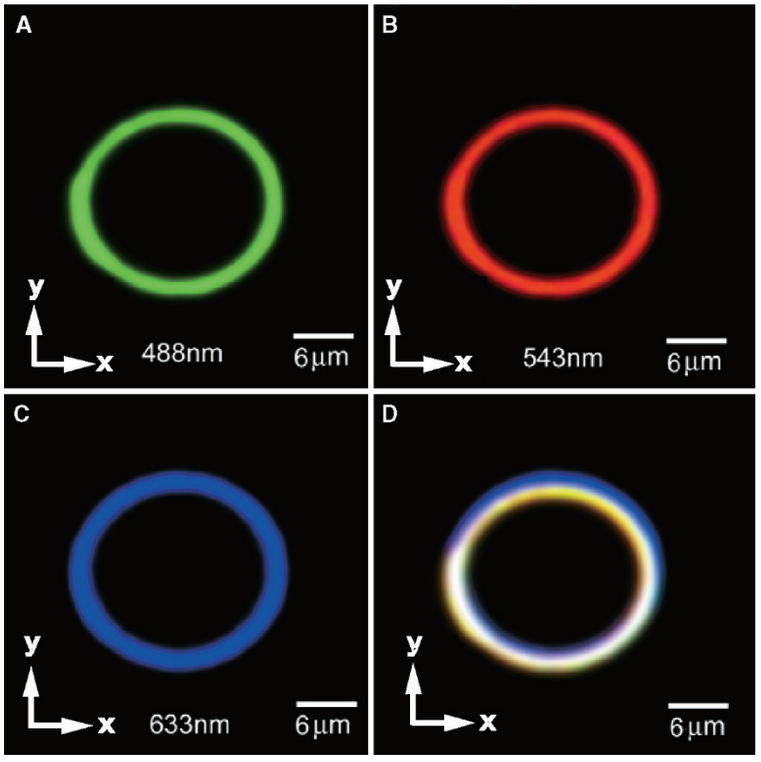

FIGURE 36.9. Lateral view of Focal Check beads in three channels. In this case, the lateral registration of channels excited by 488 nm, 543 nm, and 633 nm laser wavelengths is in agreement. All wavelengths are delivered through the same fiber-optic to the scanhead and a triple dichroic beam-splitter was used, thereby eliminating two of the primary causes of problems with lateral registration.

sequentially. When testing laser lines that are delivered to the scanning optics through separate couplings, it is advantageous to use a multi-wavelength dichroic beam-splitter to reduce the potential for ambiguity regarding the source of any displacement (e.g., dichroic vs. laser coupling alignment). By the same token, when one suspects misalignment in the beam-splitter or the dichroics, laser lines should be delivered through the same fiber or use beads that offer multi-channel emissions from a single excitation line.

Evaluation of multi-channel registration is most easily facilitated when the intensity levels are closely matched for each channel. Use an intensity profile plot through the image to determine the degree of misalignment, rather than relying on the multicolored image shown on the screen.

Axial Chromatic Registration

This type of aberration, in which the image channels shift in the *z*-axis, is described in Chapter 7. It is as important for 2D images as for 3D images. The large beads described above are not the best solution for evaluating chromatic aberration in the *z*-dimension. Due to a refractive index mismatch between the core of the bead and the fluorescent shell, the beads act as ball lenses and produce impressive (not to mention alarming) artifacts in the *z*-dimension (Fig. 36.10; also see Pawley, 2002). Axial chromatic aberration is best evaluated utilizing the same front-face mirror test used to determine axial resolution, except in this case the data from multiple laser lines are collected in separate channels. This test is very sensitive to chromatic aberration in the optical system, and even very small axial displacements of the focal plane between laser wavelengths can be quantified (see Chapter 15, *this volume*; also Akinyemi *et al.*, 1992; Browne *et al.*, 1992; Maly and Boyde, 1994).[6] Axial chromatic aberration is evaluated by plotting intensity as a function of *z*-position for multiple channels simultaneously (Fig. 36.11). A mismatch between the refractive index of the lens immersion media and the specimen can exacerbate longitudinal chromatic aberration because the spherical aberration produced by the mismatch has a chromatic component. Such discrepancies can be a major concern in resolution-sensitive multi-channel experiments.

Field Illumination

One cannot assume a correlation between signal intensity and fluorochrome concentration unless the illumination pattern is uniform across the field of view. This can be checked using a fluorescent sea (see above), fluorescent plastic slides (van den Doel *et al.*, 1998; Zucker and Price, 1999) or using reflected light from a mirror standard. At a sequence of increasing zoom levels, record the fluorescence intensity near to the coverslip interface over the field of view (FOV). Adjust the mean pixel intensity to fall within the linear response range of the digitizer.

To evaluate the data, draw a diagonal region of interest (ROI) from one corner to the opposite corner and graph the intensity values as a function of position along this line (Fig. 36.12). At low zoom, the distribution of pixel intensities should be *symmetrical*, and the hot spot should be located at the center of the field of view. At higher zoom levels, the intensity distribution should flatten out such that the values of the sampled pixels approach the mean pixel intensity integrated over the entire FOV. When this is not the case, it is likely that there is an alignment problem in the optical train (van den Doel *et al.*, 1998).[7]

[6] However, although this measurement gives some measure of lens performance, one should note that it does not measure lens performance at wavelengths between the laser lines where the fluorescent signal is actually recorded.

[7] Recently, thin-film (150 to 200 nm) fluorescent, specimens have been developed by Brakenhoff to measure the performance of optical-sectioning imaging systems (Zwier, *et al.*, 2004). These films permit standardized evaluation of illumination and signal-collection uniformity, axial resolution; spherical aberration, and off-axis chromatic aberrations in the form of sectioned imaging property (SIP) charts (Brakenhoff, *et al.*, 2005).

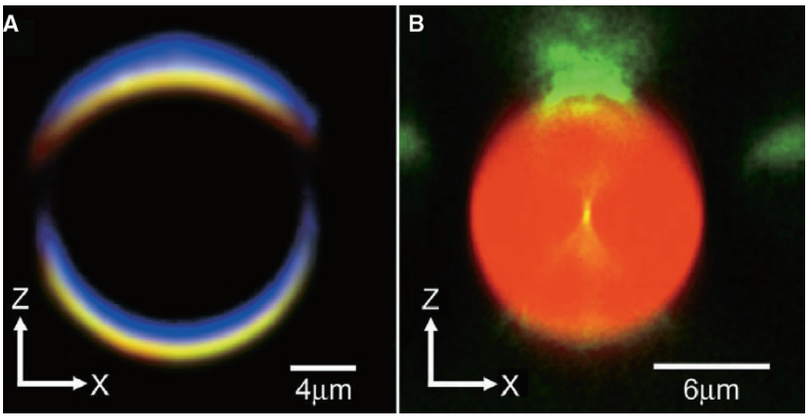

FIGURE 36.10. Self-lensing artifacts. (A) Axial view through center of Focal Check bead. Lensing by the fluorescent bead shell causes the artifact illustrated in this example. (B) Axial view through a 10 µm polystyrene sphere in both backscatter (green) and fluorescence (red) channels. Despite reasonable refractive index matching, enough of a difference exists to cause the bead to act as a ball lens. Concentrated patches of scattered light (green) are evident as a result of self-focusing.

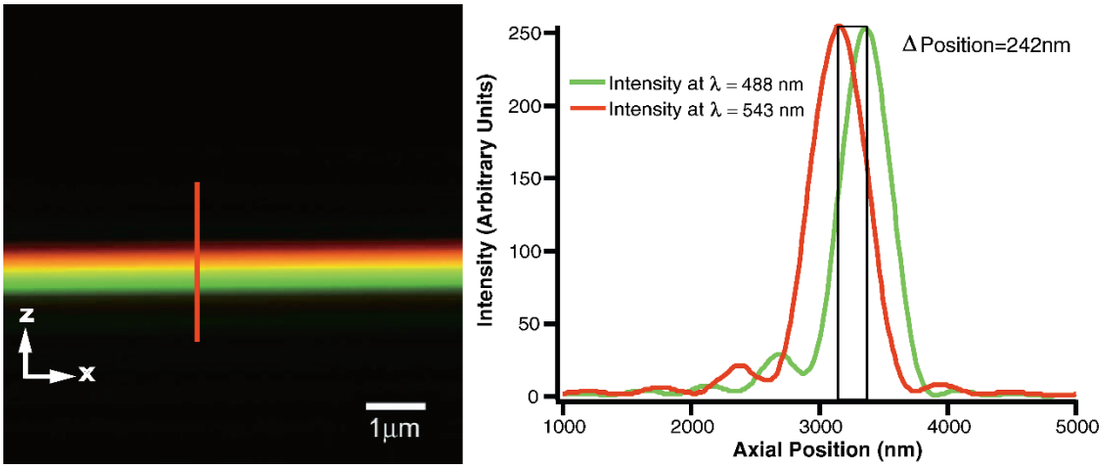

FIGURE 36.11. Chromatic aberration. In this example, a mirror standard is imaged simultaneously in two channels; the peak-to-peak distance between the first-order intensity maximum for each respective channel is 242 nm (about half the axial resolution of the lens). The wavelengths for this image were 488 and 543 nm, and a 63× NA 1.32 plan-apochromatic (oil-immersion) lens was used.

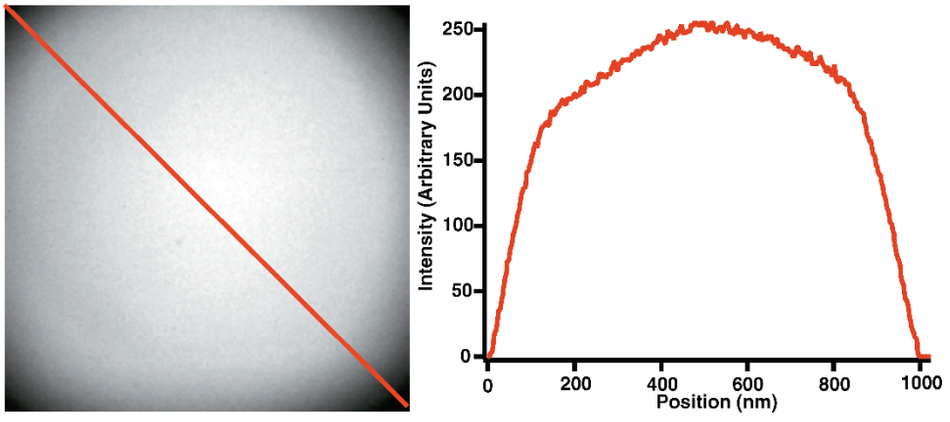

FIGURE 36.12. Flatness of field. Flatness of field is evaluated by plotting intensity as a function of position on a line drawn diagonally across the field of view (in this case the same 63× objective used above, at zoom = 1). The intensity values have been normalized for purposes of illustration in this case.

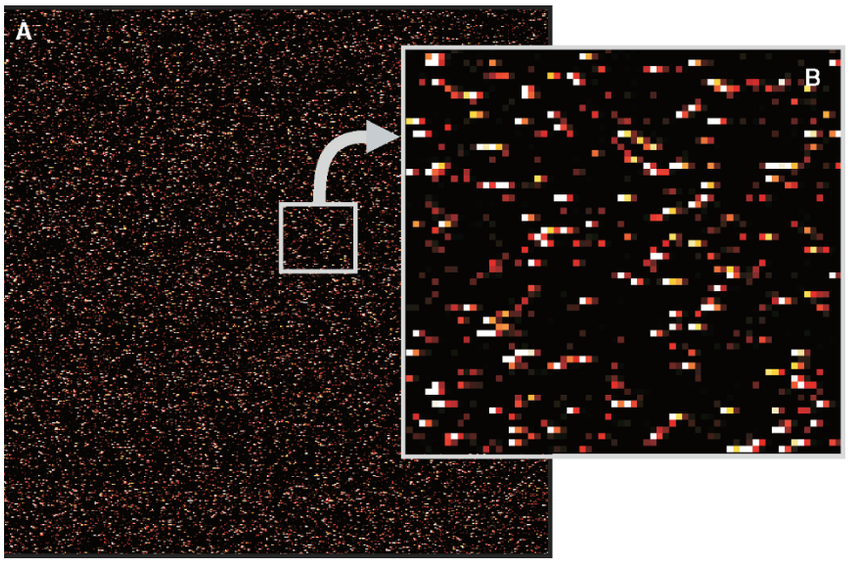

FIGURE 36.13. Instrument noise. Instrument noise may result in a speckled appearance within an image collected on a confocal microscope, although this will normally only become apparent if the instrument is used at near maximum gain or PMT voltage settings. In this example, an image was collected on a Zeiss 510 META confocal microscope with no laser light and no fluorophore present, while the PMT voltage was set to maximum (1250 V) and the amplifier gain set to 1 (the lowest setting). Panel (A) shows a 512×512 pixel image collected in a single pass, and panel (B) shows a digitally enlarged view of a small region of the image shown in panel (A). Minimal room lighting and a dark enclosure over the objective lens were used during image acquisition to eliminate the possibility of stray light entering the scanhead of the instrument. Note the relatively few high intensity pixels adjacent to a large number of very low intensity pixels. In some cases the noise is only detected in a single pixel, but in others the noise is distributed across 2 or even 3 pixels in the horizontal direction (the direction of scanning).

Signal Detection

The Signal-to-Noise Ratio and Coefficient of Variation

The sensitivity in an imaging system depends on the ratio of the signal generated by the stain and registered by the detector to the sum of all the noise signals (i.e., detector noise, stray light, nonspecific staining, etc.), as recorded under imaging conditions (see Chapters 2, 4, 22, and 35, *this volume*; also Pawley, 1994; Tran, 2005). This is referred to as *the* signal-to-noise ratio (S/N). The S/N capability of a microscope is reflected in the intensity distribution of pixels corresponding to a constant signal level. Thus, for routine evaluation, the S/N can be conveniently gauged from image data in terms of a percentage known as the **coefficient of variation** or CV (Eq. 2) measured from a known and homogeneous specimen using a fixed amount of excitation. (Zucker and Price, 2001b):

$$CV = \frac{(\sigma)}{I_{av}} 100\% \qquad \textbf{(2)}$$

where I_{av} is the mean pixel intensity and σ is the standard deviation of the pixel intensities in the measured region.

Many factors influence the signal measured by the detector on a laser-scanning confocal microscope. In order to attribute any variation *between* measurements to the detection subsystem, all of these other factors must be held constant (Pawley, 2000). Furthermore, the noise level in a confocal microscope has two fundamentally different components, the noise level of the instrumentation itself (dark noise) and photon (shot or Poisson) noise. PMTs vary in their quantum efficiency (QE), gain response, and dark-count rate, even within the same model and manufacturing lot. More to the point, some tubes break down when used with a high gain voltage and this increases their noise output substantially.[8] Strategies for evaluating and documenting the relative contributions of dark noise and shot noise under standardized conditions are described below.

Instrument Dark Noise

To determine the level of dark noise first turn on the confocal microscope and associated equipment and allow it to reach the normal operating temperature. Prevent stray light from entering the detectors by turning off room lights and shielding the objective from any light from computer monitors and other sources of ambient lighting [the laser(s) may also need to be turned off as there can be some light leakage through an AOTF filter even when set to 0% transmission]. Using standardized settings for PMT gain and offset, collect a single-scan image (Fig. 36.13). If the microscope is working properly, the small image features will actually be PMT dark noise counts. PMT noise will be displayed as a single high-intensity pixel (or sometimes 2 or 3 bright pixels, always oriented in the direction of the scan line) scattered randomly throughout the image. Changing the confocal zoom setting will usually not alter the presence or size of these high-intensity noise pixels.

When using standardized settings for scan speed and sampling resolution (pixel size), it may be wise to record the PMT dark counts for a series of increasing PMT gain voltages so that a baseline relationship between PMT gain and dark noise is characterized. The mean pixel value and standard deviation of pixel values from images of dark noise counts can be used to calculate the CV associated with standard PMT gain settings. Dark noise should be re-evaluated whenever one suspects problems with the imaging electronics.

Photon (Shot) Noise

One might expect that imaging a solution of a small molecular weight fluorophore would show a perfectly even intensity image (no variation between pixels). However, when imaging a fluorescent specimen of low quantum yield, a great deal of speckle is evident within the image (Fig. 36.14). Assuming that the PMT gain is set below the level at which electrical breakdown occurs, this non-uniformity mainly reflects the statistical uncertainty inherent in the detection of any photon signal. This uncertainty is called photon noise (shot noise; see above and Chapters 2, 4, 22, and 35, *this volume*).

[8] Because the rule of thumb states that PMT gain increases by a factor of 2 for every 40 to 50 volts of acceleration, one expects noise pulses to become bigger and more visible as the PMT voltage is increased. Breakdown is different in that it is characterized by the relatively sudden onset of greatly increased noise: not only bigger pulses, but many more of them.

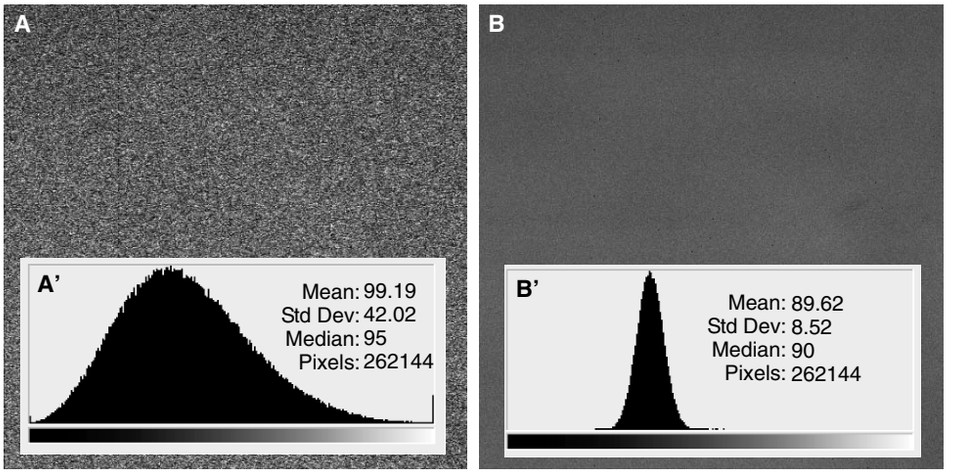

FIGURE 36.14. Demonstrating noise in images. Photon or shot noise can be seen in images collected on a confocal microscope as speckle within that part of the image where fluorescent light is being emitted. To demonstrate the effect of averaging on the level of shot noise a dilute solution of coumarin (in a sealed imaging chamber) was imaged on a Zeiss 510 Meta confocal microscope using a 60× 1.20 NA water-immersion objective. Image (A) shows a single 1 s scan with an image collection box size of 512 × 512 pixels. The whole-image intensity histogram (A′) demonstrates the wide spread of the signal (large standard deviation) due both to statistical variation in the arrival of photons at the detector and multiplicative noise in the PMT (see also Chapter 2, *this volume*). Image (B) was averaged by 16 line scans taken at the same scan speed as that shown in image (A). The whole image intensity histogram (B′) now has a much smaller standard deviation (narrower histogram profile), indicative of less variation between individual pixels within the image.

The histogram of the intensity levels within the image (Fig. 36.14) provides an intuitive way to visually assess this noise level (a broader spread in intensities results in a broad histogram). As long as the signal source is uniform,[9] the FWHM of this intensity histogram is a measure of the noise in the image. The width of the distribution can be expressed quantitatively by calculating the CV for the image.

A metric that tests the detection efficiency of imaging instrumentation is valuable for determining whether problems with image quality are due to poor specimen preparation, or to less than optimal instrument performance. With this in mind, it is useful to measure and record CV values over a range of signal intensities (Fig. 36.15) as a reference of relative detector performance at a particular point in time. Special calibration slides covered with microspheres having discrete intensity levels are available (log and linear scales; Rainbow Particle Slide, Spherotech, Libertyville, IL). Fresh dilutions of fluorochrome are a convenient alternative. Such standards could be used to record CV over a range of intensity values using a fixed laser power.

An analogous test uses a sample having a standardized quantum yield and monitors CV as a function of the laser power (Zucker and Price, 2001b). Fluorescent plastic slides are useful in this context. Most plastics behave as a highly viscous solution of fluorescent dye, which has the advantage that any photobleached areas will no longer be distinguishable from the surrounding plastic after several hours of storage. However, the fact that it is difficult to confirm that the quantum yield of fluorescent plastics is stable over long-term use introduces uncertainty into quantitative comparisons of instrument performance over time. In addition, as the RI of the plastic is not one for which objective lenses are normally corrected, spherical aberration will reduce the recorded signal significantly as one focuses further into it.

[9] That is, not only no visible features but not even any shading such as might be caused by signal loss at the edges of the field of view. This condition is more easily met by using a medium zoom.

PMT Linearity

To establish that the relationship between the signal digitized from the PMT responds linearly with the fluorescence signal produced by the specimen, first prepare a fresh standardized dilution of flu-

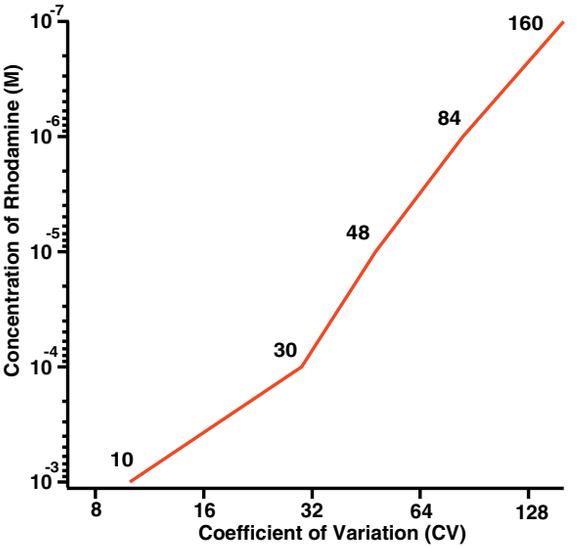

FIGURE 36.15. Detector response to decreased signal. Coefficient of variation as a function of fluorochrome concentration. CV values were taken from the spectral image that corresponds to the peak emission range (568–573 nm) at minimal bandwidth (5 nm) using a spectral detection system. The series is a 10-fold dilution of Rhodamine 6G; the laser power was held constant and the PMT gain was increased at each reduction in concentration to maintain a mean signal of 130 A.U. (scale 0–255). The PMT gain was maximized (1000 V) at a 10^{-6} dilution. At the lowest concentration (10^{-7}), the system is unable to produce a mean signal above 50 A.U. As the PMT gain is already maximized at a dilution of 10^{-6}, the decreased signal is responsible for the increase in apparent noise at the lowest concentration.

orochrome in the appropriate refractive index solvent. Then adjust the PMT gain setting to give a signal within the linear response range and finally record the mean signal as a function of the illumination intensity. The mean brightness should be proportional to laser power until the laser becomes so bright that the molecules in the focused spot are driven into singlet-state saturation (i.e., so many of the molecules are in the excited state that there is no dye left to excite;[10] see Chapters 2, 16, and 35, *this volume*). Approaching saturation will produce a less than proportional increase in signal for an increase in excitation. Although the effect of saturation can be reduced by going to a lens with lower NA because this makes the spot bigger and the light less intense, you then have a dry lens and all the SA problems associated thereto. One should validate the performance of the detector subsystem periodically as the instrument gets older.

Spectral Systems

An exciting development in laser-scanning microscopy is the increasing availability of signal detection systems capable of recording crude emission spectra at each pixel in an image. Evidence of the ability of such systems to solve problems, such as distinguishing the identity of overlapping emission profiles, has been established (Dickinson *et al.*, 2001; Lansford, *et al.*, 2001; LaMorte *et al.*, 2003; Huth *et al.*, 2004; Hutter, 2004). The accuracy of such extrapolations is dependent on the accuracy and reliability of the underlying system (Garini *et al.*, 1999; Neher and Neher, 2004; Zucker and Lerner, 2004).

Spectral detection devices can be made in several ways. The advantages of a particular system will depend on the scope of applications an instrument is expected to handle. As all such systems are complex (and expensive!) compared to traditional filter-based systems, finding a convenient strategy to evaluate their performance is of prime importance.

Three major aspects of the spectral imaging subsystem should be periodically evaluated: (1) calibration accuracy of the system (wavelength accuracy), (2) resolution in terms of the minimum resolvable bandwidth, and (3) variation of sensor efficiency with wavelength.

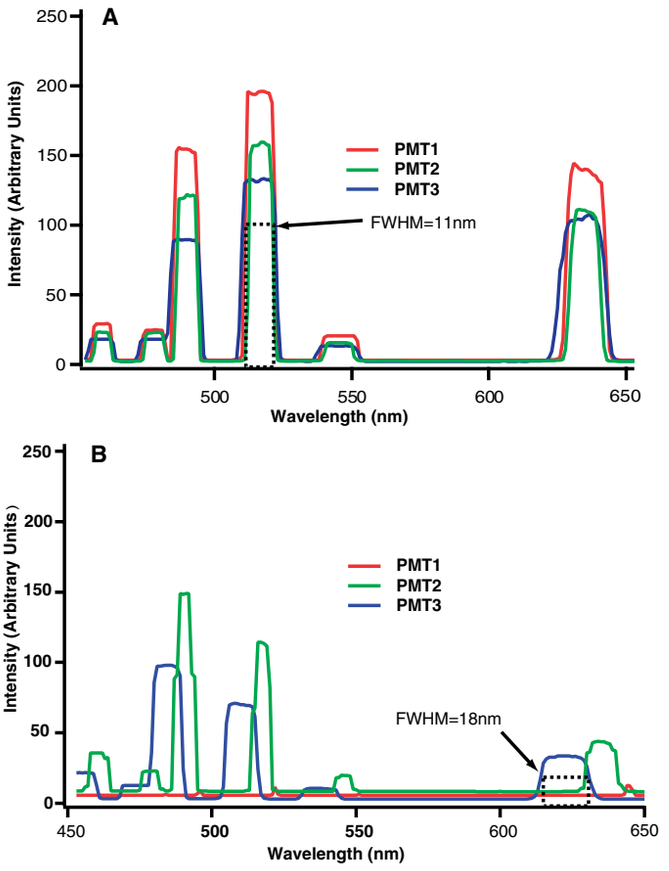

FIGURE 36.16. Spectral scan over laser lines using reflected light. (A) A typical plot for a spectral imaging instrument working correctly. The signature for the laser lines are centered about the appropriate wavelength and the spectral resolution (FWHM) is close to 10 nm. (B) A malfunctioning system. The wavelength selection mechanism for PMT 1 is inoperable, hence the low signal for that channel. The spectral reading for each channel is centered about a different wavelength and the spectral resolution approaches 18 nm in places.

Spectral Accuracy

The best way to test accuracy is to image a standard that displays narrow peaks in known locations. When doing these tests, all sources of extraneous light (overhead lamps and computer monitors) that might contaminate the spectrum of the illumination source should be masked (often a black velvet shroud or a black box can be carefully placed over the imaging area). Using the reflected light from a mirror test slide and a high zoom to avoid off-axis aberrations, the lasers installed on the system can be used as a convenient source of monochromatic light. In order to check the accuracy of spectral registration, it is advantageous to use as many laser lines as possible. PMT gain voltage should be adjusted such that the magnitude of the intensity peak reflected from the strongest laser line is within the linear response range of the PMT/digitizer. Acquire a high-resolution spectral scan over the visible spectrum, and observe the location of the spectral features corresponding to the laser wavelengths. This can often be recorded as a plot of intensity versus wavelength [Fig. 36.16(A)]. If the peaks are not where they are expected [Fig. 36.16(B)], either the detector is miscalibrated or one or more of the system components has failed.

Alternatively, if the laser lines available don't properly cover the full wavelength range, one can use an NIST-certified multi-ion discharge calibration lamp (MIDL, LightForm Inc., Hillsborough, NJ) in the manner described by Zucker and Lerner (2004). In this approach, a lamp with very well-characterized peaks in its spectral output is placed directly above the objective being used for measurement, and a spectral reading is taken using the acquisition subsystem of the microscope. The NIST calibration lamp has numerous spectral features that form a sophisticated spectral fingerprint. In theory, all instruments should reproduce the characteristic set of relative heights of peaks and valleys provided by the standard. The effect of under-sampling in the wavelength dimension on the accuracy and precision of the recorded spectra is easily demonstrated using this standard (see Chapter 4, *this volume*; also Zucker and Price, 2001b).

Spectral Resolution

The resolution is indicated by the FWHM of peaks in spectra derived from subresolution spectral features (such as monochromatic laser output). Presently, most systems are designed for 2 nm

[10] Because the degree of saturation varies throughout the PSF, this saturation is not a "hard" effect in the sense that an absolute limit is reached and no further increase is possible. Rather the signal increases asymptotically as the degree of saturation increases at ever greater distances from the center of the PSF.

to 10 nm bandwidth resolution, with the value for each particular system available from the manufacturer. When spectral resolution values are less than expected [Fig. 36.16(B)], the boundaries of virtual filter bandpass settings may be offset to some degree unknown to the operator (in the case of the Leica, the moveable mirrors may be miscalibrated or stuck in one position). Such errors produce much higher background than expected because, under imaging conditions, scattered light from the laser can reach the detector. Data collected with poor or shifted spectral resolution can also produce anomalous fluorochrome localization results when treated using spectral deconvolution algorithms.

Wavelength Response

The reflected laser light test paradigm outlined above can be used to provide an expedient measure of sensor response in different wavelength regimes; anomalous sensor response with respect to frequency will seriously affect the accuracy of spectral un-mixing schemes. Fingerprints or other contamination on certain mirrors within the detection system can easily cause diminished response in part of the spectrum. In this test, the relative laser powers for all the individual lines used are known. First, the laser lines are individually adjusted to some standard value (e.g., 15 µW, emerging from the same dry objective) then the PMT gain and offset are configured so that the entire intensity range is within the linear response range of the PMT(s). A spectral scan is taken across the part of the spectrum containing the laser lines. On the resultant plot of intensity versus wavelength, the intensity values measured for the laser lines should be of roughly the same magnitude,[11] and the mean value of the noise level should remain constant in the domains between laser lines. On systems with multiple spectral detectors, each detector should be checked in turn. A method for performing the equivalent test using the NIST standard lamp is discussed in Zucker and Lerner (2004).

The uniformity of the response of a spectral detector can be assayed by collecting a spectrum from the light transmitted through a microscope slide from the transmitted light source. Assuming that this source uses a tungsten/halogen bulb, apply the correct voltage to heat the filament to 3400 K, and set the condenser for Köhler illumination. If you now collect a spectrum with the laser turned off, it should slope from higher in the red to lower in the blue. When recorded on the Zeiss, META, valleys in this spectrum probably correspond to individual micro-PMTs that have lower than average gain or QE. Although this is to be expected, it is the reason why it is better to collect reference spectra using the specific setup that will be used for the experiment, rather than relying on stored spectra that were obtained at the factory. This same transmitted light setup can be use with a Hg-arc source that provides additional calibration lines (see Chapter 4, *this volume*).

OPTIMIZING MULTI-LABELING APPLICATIONS

Confocal microscopy is ideally suited to multi-labeling applications due to the ease and flexibility with which multiple fluorophores can be viewed and recorded as separate images. This includes the more traditional spectral separation of fluorescence from different dyes as well as the ability to separate highly-overlapping fluorophores using spectral unmixing.

Control Samples Establish the Limits

The relationship between the fluorescence intensity data content of an image and the distribution of the fluorophore of interest in the sample can only be verified by collecting reference images from the correct controls. Controls are also essential for establishing the detection limits.

Establishing the Level of Autofluorescence

Fluorescence emission from a sample to which you have not yet added a fluorophore is termed autofluorescence (for further discussion, see Chapters 8, 21, 44, *this volume*). Many naturally occurring compounds in plant and animal tissues will fluoresce, and various cellular treatments, including the media in which they are grown and the physical manipulation (including the method of fixation), may influence the intensity and wavelengths of emission.

An unlabeled control is essential for establishing the level of autofluorescence in the sample. Additional images of the unlabeled control collected with increased detector gain, pinhole size, or excitation power can be used to establish the upper limit of detection of your fluorophore. However, even a high level of autofluorescence is not necessarily a problem, as long as the intensity, location, or the spectral characteristics of the probe can be distinguished from autofluorescence.

Is Reflected Light Contributing to Your Fluorescence Image?

The level of signal intensity from an unlabeled control is also essential for establishing the level of backscattered or reflected light that is contributing to the image (Pawley, 2002). Any excitation light that is reflected or backscattered back toward the detector will be registered as a signal unless the barrier filter stops it. Even the very best barrier filters are not 100% efficient; and because the intensity of illumination is several orders of magnitude higher than that of the fluorescence signal even very small percentages of reflected light passing through a barrier filter may be of similar intensity to that of a fluorescent signal. Small refractile features that produce much backscattered light may also appear to show specifically labeled subcellular detail. A useful test for distinguishing contributions from backscattered illumination compared to autofluorescence is whether or not one detects a uniform background signal level as the focus plane coincides with the surface between the coverslip and the aqueous media. While such a signal can be a handy marker for the location of the glass surface, it is also an indication that some of the signal recorded in this channel stems from backscattered light.

How Much Is Bleed-Through Contributing to the Image?

Bleed-through is the appearance of fluorescence from one fluorophore in the detection channel set up to detect another fluorophore. The amount of bleed-through is determined by imaging control slides in which only one dye is present while using the dual-channel settings you plan to use for your dual-labeled samples. Images collected at various gain, pinhole, and laser intensity levels may be useful for establishing the amount of bleed-through at various settings. This information should be used to set limits for the various settings that will result in an acceptably low bleed-through level.

[11] There are two offsetting factors at work here. If the photometer is calibrated for the measured wavelength, then 15 µW will correspond to more red photons than blue photons. As the output of the PMT is proportional to the number of electrons produced at the photocathode, one might expect that the PMT would produce more signal from the red beam because it has more photons. However, this tendency is usually more than cancelled out by the fact that the QE of the PMT drops at longer wavelengths.

How Much Is the Secondary Conjugate in Immunolabeling Contributing to the Signal?

Secondary conjugates (including avidin/biotin systems as well as secondary antibodies) often contribute to background signal in immunolabeling procedures. Application of fluorescently-labeled secondary conjugate, in the absence of its target primary antibody, is an essential control in all immunolabeling experiments. The contribution of the secondary conjugate to the fluorescent signal is determined by imaging a sample labeled using the secondary conjugate alone under the same conditions as employed for the experimental sample. In addition, as discussed above for autofluorescence, images collected at increased detector gain, pinhole size, and laser power, will be useful for establishing the limits to detection for the binding of your primary antibody.

A Positively Labeled Sample

It is a great asset to have a cell or tissue sample, or an environmental/metabolic condition that you know will produce a positive response for your target molecule. This can assist in establishing the probe concentrations, imaging conditions, and the instrument settings that can be used on your experimental sample. A positive control closely related to your test sample (e.g., the same cell line, but stimulated to produce a known positive response) is an ideal model of the labeling and imaging conditions used for the experimental sample. A known positive is particularly important when troubleshooting problems with an immunolabeling protocol.

Separation of Fluorescence into Spectral Regions

Traditionally, one images multiple fluorophores by using interference filters to separate the fluorescent light into different spectral regions. Although the use of dichroic mirrors and optical filters has the advantage of being a robust and relatively simple technology, the regions of the spectrum directed to individual channels is constrained by the availability of suitable mirrors and filters.

Another way to separate the fluorescent light into different spectral regions is to use a prism or diffraction grating to separate the light spatially and to then use either a mirror/slit mechanism or photomultiplier tube array to select the region of the spectrum that will be digitized in each channel. This type of spectral separation has the advantage that the operator has full control of the region of the light spectrum directed to each channel, without being constrained by the available optical filters. A variety of light separation approaches are used by different confocal microscope manufacturers, sometimes more than one approach being incorporated into a single instrument.

Spectral unmixing, described in detail below, is a method of separating the signals from various fluorophores based on their spectral profile, rather than by their presence or absence in a specified spectral window. Spectral unmixing has the important advantage that fluorophores with highly overlapping spectral emission profiles can be separated into individual channels.

Sequential Channel Collection to Minimize Bleed-Through

Bleed-through occurs predominantly when multiple fluorophores are excited simultaneously and portions of their emission spectra overlap with the spectral region accepted by more than one channel. Simply exciting and collecting each channel sequentially, sometimes called multi-tracking, is a very practical means of substantially reducing bleed-through. Although this can be done on older confocal systems that use slow, motor-driven filter wheels to switch laser lines, newer systems using acoustic-optical devices (AOD) are far more flexible and allow nearly instantaneous laser line selection. This allows sequential channel acquisition to become practical for routine use. Some instruments are capable of line-by-line multi-tracking, where one wavelength is used to excite the sample as the beam travels in one direction and the second marker is excited by a different wavelength on the return scan. Although faster, one must adjust the instrument (sometimes called phase control) to ensure that the digitizer stays in synch with the position of the galvanometer mirror. Otherwise the two sets of data can be displaced horizontally from each other.

Spectral Unmixing

Spectral unmixing is a computational method of separating the signals from various fluorophores based on their spectral profile rather than by their presence or absence in a specified spectral window. Spectral unmixing has the important advantage that the fluorescence from fluorophores with highly overlapping spectral emission profiles can be reliably separated.

In spectral unmixing, the emission spectrum of each fluorophore is characterized in the form of a plot of its fluorescence emission intensity as a function of wavelength. Because the shape of this emission profile is assumed to be fairly stable,[12] one may infer the magnitude of signal that would be detected on-peak using a portion of the emission signal that was measured using a spectral window located on the tail of the spectrum. Multiple samples of the signal intensity taken over the entire the emission profile may provide an even more accurate estimate of the peak signal.

It is then possible to use a deconvolution operation to separate overlapped spectra in a manner analogous to the way in which spatial deconvolution is used to separate overlapped structural features. The process starts with the collection of a reference spectrum from each positive control sample.[13] Next, spectral data is collected at each voxel in a 2D or 3D image. To unmix the data, the computer fits the measured data to a weighted sum of the reference spectra. Spectral unmixing can be performed on as few as two spectral windows of the emission spectra at each pixel, but using data from multiple spectral windows at each pixel greatly improves the degree of separation that can be achieved.

Spectral Unmixing to Separate Overlapping Fluorophores

In Figure 36.17, live cells labeled with acridine orange have been imaged using two conventional channels on a Zeiss Meta confocal microscope. The green fluorescent light (500–530 nm) has been directed to one channel [Fig. 36.17(A)] and the red fluorescent light (565–615 nm) has been directed to a second channel [Fig. 36.17(B)]. Although the two channels do show some differences, the high degree of overlap is evident by the yellowish color that

[12] There are lots of counterexamples, such as carboxyfluorescein, that changes its output spectrum in response to the environment, such as changes in pH.

[13] Although the manufacturer often provides such spectra for common dyes, these will only be accurate to the extent that (1) the QE/wavelength curves of the detectors used in the factory are the same as those on your machine; (2) the dye spectra has not been modified by the local environment; and (3) your system remains aligned.

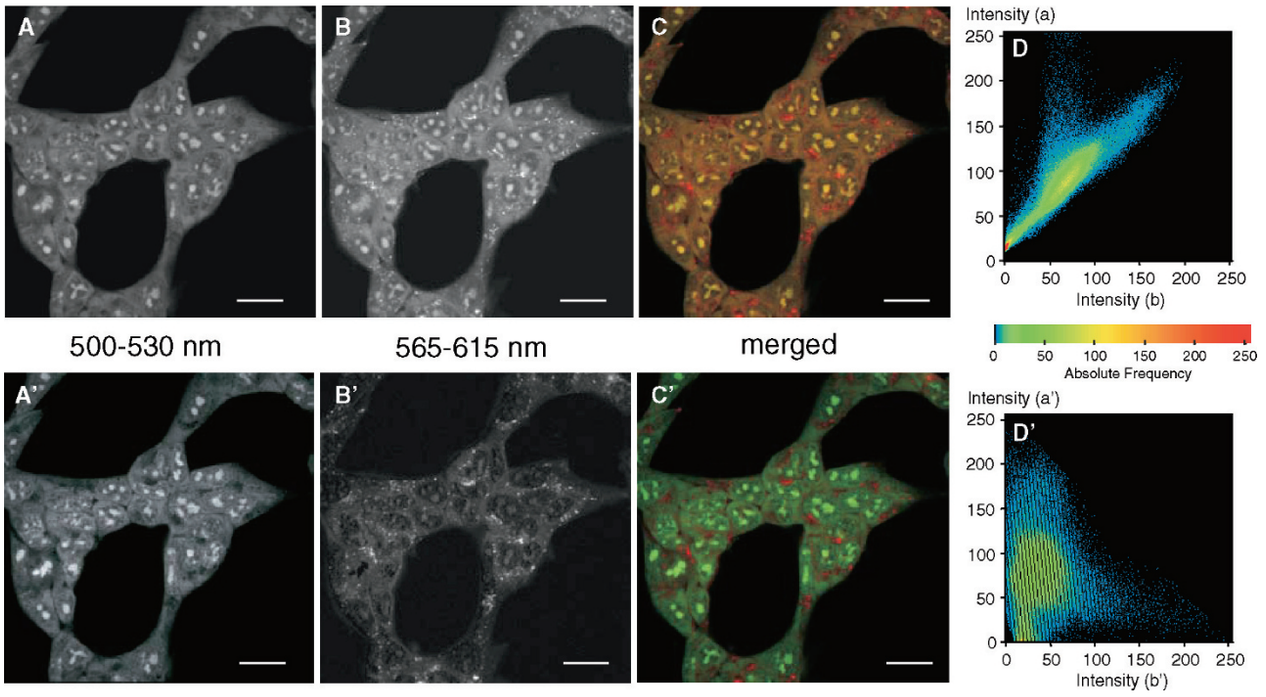

FIGURE 36.17. Spectral separation using two spectral images. The process of linear unmixing can be used with as few as two spectral images to improve the separation between the two channels. In this example HEK496 cells have been labeled with Acridine Orange (final concentration 0.5 µg/mL) for 1 h at room temperature and images were collected on a Zeiss 510 Meta confocal microscope using two "conventional" optical filter separation channels. Images were collected from (A) the green (500–530 nm) region of the light spectrum and (B) the red region of the spectrum (565–615 nm). A merged two-color image of the green and the red channel is shown in (C). In (D) a fluorogram of the two channels is shown. The corresponding images after spectral reassignment are shown in (A′) green (500–530 nm), (B′) red (565–615) nm. and both channels merged (C′). (D′) A fluorogram of the reassigned merged image is shown in (C′). There is considerable overlap between these two original imaging channels, which is shown graphically in the scattergram shown in (D). Applying the process of linear unmixing (using the Zeiss LSM 510 Meta software) the separation between these two channels has improved [(A) and (B)], which is shown by comparing the fluorogram before (D) and after linear unmixing (D′). The scale bar represents 20 µm.

predominates in the merged image [Fig. 36.17(C)]. This overlap is also shown by the tight central location of the dots in the whole-image intensity histogram [Fig. 36.17(D)]. However, after linear unmixing of these two images, the difference between the two images becomes more distinct [Fig. 36.17(A′,B′)]. A merged two-color image of the two reassigned channels [Fig. 36.17(C′)] clearly shows that a population of vesicles has now been separated from the bulk of the staining. Spectral reassignment has resulted in a significant movement of red and green pixels towards their respective single label axes [see the greater spread of the pixel intensity histogram in Fig. 36.17(D′) compared with Fig. 36.17(D)]. However, the separation is by no means complete as the majority of structures are still being detected in both channels.

Figure 36.18 demonstrates that multiple spectral images permit an even more refined separation of subcellular structures. In this experiment, 10 individual spectral images (each with a spectral window of 21.4 nm) [Fig. 36.18(A)] were collected using two sequential scans on a Zeiss 510 Meta confocal microscope (up to eight spectrally distinct images can be collected simultaneously). These 10 images are then analyzed as a "spectral stack" [Fig. 36.18(B)], and four separate regions of the image stack are highlighted with a numbered cross. The spectral information from each of these regions is shown graphically in Figure 36.18(C). Using this graphical display of the four different spectra found within the sample, two spectral regions, green (504–569 nm), which predominantly covers the spectral emission of ROI 2 to 4, and red (591–719 nm), covering ROI 1 have been chosen for the extraction of two channels [Fig. 36.18(D)]. The population of small vesicles with a spectral emission consisting predominantly of red fluorescence can be clearly distinguished from the structures emitting in the green region of the spectrum. However, the separation of the red vesicles from the rest of the cell is not complete; the majority of the red vesicles also contain green pixels [seen as yellow/orange pixels in the merged image of Fig. 36.18(D)].

The spectral information shown graphically in Figure 36.18(C) can be used to locate and extract other regions of the specimen having a similar spectral fingerprint using linear unmixing. In this case, the software has separated the stack into four separate channels [Fig. 36.18(E)] plus a residual channel (regions of the stack that cannot be assigned using spectral information from the selected areas). The merged two-color image of channels 1 and 3 [Fig. 36.18(E)] shows two distinct populations of vesicles clearly separated from any background fluorescence. The vesicles that were partially separated from the other cellular labeling using conventional optics [Fig. 36.17(A,B)] or channel extraction from the spectral stack [Fig. 36.18(D)], as described above, have now been separated into two distinct subpopulations that are also separated from other subcellular structures. This example shows that spectral imaging can be used both to separate the fluorescence from different overlapping signals into separate channels, and also to

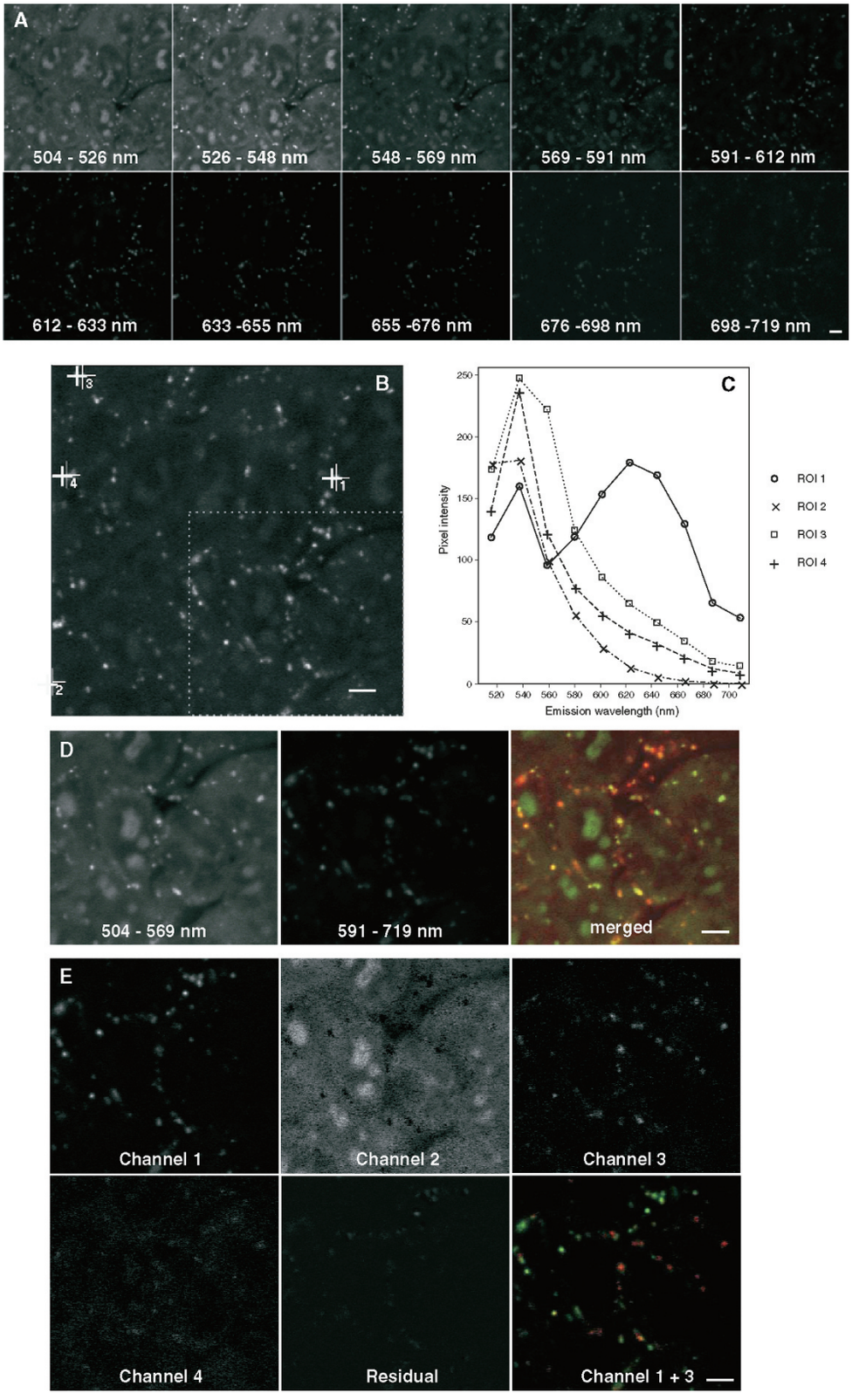

FIGURE 36.18. Spectral separation using multiple spectral images. Linear unmixing using multiple spectral images results in better separation of fluorophores with overlapping emission spectra. HEK496 cells were labeled with Acridine Orange (final concentration 0.5 µg/mL) for 1 h at room temperature and multiple spectral images were collected (A) from 21.4 nm wide regions of the light spectrum using the Meta channel on a Zeiss 510 Meta confocal microscope. The 10 spectral images were analyzed as a spectral stack (B) and the spectra extracted from four specified single-pixel regions of interest (ROI, marked with + in the spectral stack) are shown in (C). Two defined spectral regions (504–569 and 591–719 nm) were selected and the spectral information extracted into separate channels (D). Four spectrally-reassigned channels plus a residual channel after linear unmixing are shown in (E). The scale bar represents 5 µm.

collect and recognize the spectral fingerprint of specific structures within the sample.

Removing Autofluorescence Using Spectral Unmixing

Two different approaches to separating autofluorescence from the signal produced by an added label can be employed. The first approach is to treat the autofluorescence as an endogenous fluorophore that will be placed in a separate channel after linear unmixing. This approach works well when the autofluorescence is dominated by a single endogenous fluorophore. Unfortunately, this is rarely an accurate assumption. Another approach to unmixing autofluorescence from specific labels is to use spectral profiles from the fluorophore positive controls for spectral unmixing, and to assign any measured fluorescence emission that does not fit these reference spectra to a "residual channel" [Fig. 36.18(E)]. In this way complex spectral emission due to autofluorescence can often be separated from the more specific emission associated with the particular probes added. However, caution is needed to prevent "seeing what one wants to see," especially when the level of Poisson noise is high.

Limitations to Spectral Unmixing

Even though spectral unmixing has a remarkable ability to separate similar fluorescence emission spectra, there are disadvantages that should not be overlooked. Spatial deconvolution (see Chapters 25, *this volume*) can help improve the integrity of results from spectral unmixing. The procedure would be to spatially deconvolve or at least Gaussian filter[14] the data from each wavelength segment prior to unmixing.

Poisson uncertainty (see Chapters 2, 4, and 35, *this volume*) places severe restraints on the accuracy with which spectral unmixing can be carried out. Supposing that a particular dye produces 100 ± 10 detected photons/voxel, if these are then shared among only four channels of a spectral detector, the signal drops to 25 ± 5 or 20% noise. It is also notable that the *effective* QE of the mini-PMT arrays used in some systems is lower than that found on many standard PMT tubes used in confocal microscopes. Furthermore, the layout of the very small electron multipliers that they contain precludes taking actions that would reduce multiplicative noise. Thus, contributions from both Poisson noise and multiplicative noise to the uncertainty of spectral unmixing may be exacerbated by detector design.

The collection of spectral information frequently necessitates the collection of several images in series, which may subject the specimen to damaging doses of light.

Another potential problem is that the composite spectrum may be distorted because any segment of the spectrum that overlaps a dichroic mirror blocking range will exhibit a prominent dip in the signal intensity. In addition, if the spectra being collected overlaps with an active laser line, excessive backscattered light may contaminate the signal.

Environmentally caused variation in the spectral characteristics of a fluorophore may lead to the inappropriate signal separation. Many fluorophores, such as Acridine Orange, as used in the example above (see also Chapter 39, *this volume*), can respond differentially to environmental influences.

[14] Because the data is so noisy and the PSF of a confocal or multi-photon microscope is so simple, 3D Gaussian filtering and deconvolution have much the same effect. Gaussian filtering can also be applied to 2D data, a point that is important because much unmixing work is carried out on 2D data.

COLOCALIZATION

Colocalization is a tool for quantifying the degree of association or codistribution of labeled structures between any two channels in an image. Although colocalization is a very powerful tool for determining subcellular associations, even under ideal imaging conditions the resolution limit of light microscopy severely constrains the validity of any colocalization analysis.

Image Collection for Colocalization

Colocalization by counting overlapping signals is very sensitive to intensity imbalances between each channel, as are methods utilizing channel subtraction and cross-correlation analysis (for discussion see Manders *et al.,* 1993; Costes *et al.*, 2004). As the initial assessment of the degree of colocalization often relies on a quick visual inspection of a merged two-channel image, it is advisable to always collect relatively balanced signal intensities for each channel. Signal balance is also important so that spread of the signal outwards from the highest intensity areas does not bias the results. This phenomenon is particularly noticeable in small structures with one or more dimensions close to the resolution limit of the microscope.

Fluorophore selection is an important part of any colocalization study, and is discussed in detail by Smallcombe (2001). Suitable pairs of fluorophores should have a wide separation between their emissions or bleed-through between collection channels will be registered as colocalization, no matter which method of analysis is used. Filter selection (see Chapter 3, *this volume*) and proper controls (discussed above) are crucial for the validity of any colocalization analysis. Single image planes from any volume should be examined carefully before any attempt at quantification. Noise and all sources of background (e.g., blur, autofluorescence, nonspecific labeling, reflections, and bleed-through) have a major impact on the quantification of colocalization (Manders *et al.*, 1993). Optical misalignment of the instrument will also have a big impact on the apparent degree of colocalization. As a general rule, problems of image quality should be addressed at the time of data collection, rather than by postprocessing. Providing the guidelines for Nyquist-pixel sampling have been observed and the raw data has been 3D spatially deconvolved or 2D filtered to remove "single-pixel noise" (see below and Chapter 4, *this volume*), the validity of colocalization analysis is constrained by the resolution limit of light microscopy.

Complex images should be examined carefully, and specific regions or structures within the image analyzed in detail before attempting to quantify the degree of colocalization. Information on the biology of the sample will be of great value in determining the approaches taken to quantifying the degree of colocalization. Projection images from optical volumes cannot be utilized for colocalization because pixels mapped to the projection image may have originated in planes displaced axially by several microns.

Temporal resolution should not be overlooked when using sequential imaging on living cells. This is particularly important when sequential frame scanning, but even when sequential line scanning, or using a CCD camera on high-speed Nipkow disk systems, a delay of as little as 100 ms between channels can allow a structure to change position in resting cells, this includes the normal movement of vesicles, organelles, filopodia, or neuronal growth cones. The temporal sampling rate becomes more critical when attempting colocalization of more dynamic processes. The result, of course, is that instead of observing a possible colocal-

ization event, one observes the structure as single-labeled and spatially separated in two separate channels.

Quantifying Colocalization

The 2D histogram, sometimes called a fluorogram, is a powerful tool for exploring the relationship of the intensities between two channels in an image (or within a defined region of the image). The 2D histogram is a scatter plot with the intensities of all the pixels in one image channel plotted along the *x*-axis versus the intensities of the same pixels in the other channel plotted along the *y*-axis (Demandolx and Davoust, 1995, 1997). For example, in Figure 36.20, the green channel is plotted along the *y*-axis and the red channel is plotted along the *x*-axis, with 0 at the origin. Given equal background levels in the channels, pixels possessing nearly equal intensities in both channels would plot along a 45° line passing through the origin, similar to the distribution in the fluorogram in Figure 36.17(D). Custom color tables can be useful to highlight potential colocalizations when working with rare events or imbalances in channel intensities (Demandolx and Davoust, 1997; Agnati *et al.*, 2005).

The most commonly employed algorithms for quantifying colocalization measurement are derived from Pearson's correlation coefficient, first applied for this purpose by Manders and colleagues (1992). The Pearson's coefficient, *R*, describes the correlation between the intensity distribution, or pattern overlap, in two channels in terms of a least-squares fit (Eq. 3). This value can be between −1 and 1, where $R = -1$ indicates complete exclusion and $R = 1$ indicates complete correlation between the two channels. Values between 0 and 1 indicate a proportional degree of overlap between the two channels. Values between −1 and 0 are ambiguous, indicating some form of inverse relationship between the channels, as may occur when one channel is very dim and the other is bright, or even when non-overlapping.

$$R = \frac{\sum_i \left(S1_i - S1_{avg}\right) \times \left(S2_i - S2_{avg}\right)}{\sqrt{\sum_i \left(S1_i - S1_{avg}\right)^2 \times \sum_i \left(S2_i - S2_{avg}\right)^2}} \quad \textbf{(3)}$$

where $S1_i$ is the intensity of the *i*th pixel in channel 1; $S1_{avg}$ is the average intensity of all pixels in channel 1; $S2_i$ is the intensity of the *i*th pixel in channel 2; and $S2_{avg}$ is the average intensity of all pixels in channel 2.

Other coefficients have been subsequently derived to provide additional information regarding the nature of the colocalization, as well as providing less sensitivity to channel imbalances (Manders *et al.*, 1993). The overlap coefficient, *r*, describes the degree of overlap between the signals on a range of 0 to 1 (Eq. 4)

$$r = \frac{\sum_i (S1_i \times S2_i)}{\sqrt{\sum_i (S1_i)^2 \times \sum_i (S2_i)^2}} \quad \textbf{(4)}$$

This coefficient provides a significant result only when the number of colocalizing objects in both channels is greater than zero. The advantage of this coefficient is that, unlike *R*, it is not as affected by differences in intensities between the channels, reducing the impact of channel imbalance. Although the overlap coefficient has these advantages, the Pearson's coefficient is less sensitive to image background levels. Both of these coefficients, *R* and *r*, are affected by the relative number of labeled objects (or voxels) in each channel of the image.

The colocalization coefficients *M*1 (Eq. 5) and *M*2 (Eq. 6) are often the most biologically useful, representing the proportion of pixels from each channel that contribute to the colocalized area. They can be determined regardless of the balance between the number of pixels colocalizing in each channel or between the average intensities of the two channels. The only limitation is that there must be some colocalization present.

$$M1 = \frac{\sum_i S1_{i,coloc}}{\sum_i S1_i} \quad \textbf{(5)}$$

where $S1_{i,coloc} = S1_i$ *if* $S2_i > 0$ and $S1_{i,coloc} = 0$ *if* $S2_i = 0$

$$M2 = \frac{\sum_i S2_{i,coloc}}{\sum_i S2_i} \quad \textbf{(6)}$$

where $S2_{i,coloc} = S1_i$ *if* $S1_i > 0$ and $S2_{i,coloc} = 0$ *if* $S1_i = 0$.

Each numerator represents colocalized pixels — the sum of intensities from pixels within one channel that also contain some intensity component from the other channel. The denominators constitute the summed intensities of all pixels, above threshold, in the channel. Some software applications use upper- and lowercase to distinguish colocalization coefficients calculated from the global image from those calculated from a thresholded image or a region selected from the fluorogram.

Setting Thresholds

Quantitation in colocalization studies is usually dependent upon the subjective application of thresholds. Establishing the threshold to eliminate noise or background is sometimes carried out by subtracting the threshold from the image, or by setting limits in the 2D histogram, which many find to be more intuitive. One may have to test multiple thresholds before finding the levels that are supported by correlative methods and the controls. When software recommends threshold settings (or setting background levels), it is important to know how those settings are being calculated. A background derived from the darkest pixels within the image more correctly represents the noise floor of the image rather than the amount of background from bleed-through, autofluorescence, or non-specific labeling. A new approach has been developed that estimates thresholds for both channels simultaneously over a range of decreasing thresholds until the probability of correlation equals zero (Costes *et al.*, 2004). This approach promises to be less subjective, but can be still skewed by an imbalance in average channel intensities.

Spatial Deconvolution in Colocalization Studies

Noise and background in colocalization can be reduced by employing restorative deconvolution (Van Steensel *et al.*, 1996; Landemann, 2002; Landmann and Marbet, 2004). Even analysis intended for 2D images can benefit from deconvolution if the data is collected as a shallow *z*-series and the single 2D image selected following deconvolution of the *z*-series. Alternatively, 2D confocal images can be Gaussian filtered if sampled adequately.

In the example shown in Figure 36.19, a field of peripheral nerves in rat tooth pulp is shown as a single optical slice from a *z*-stack collected at low resolution [Fig. 36.19(A)], with a small region of the sample [small box in panel (A)] shown at higher optical resolution [Fig. 36.19(B)]. The arrowhead points to the same fiber in both panels. Panel (B) indicates that there are actually two populations of closely intertwining nerve fibers, larger fibers predominantly labeled red (arrowhead), and the smaller, somewhat beaded fibers labeled green (arrows). Closer examina-

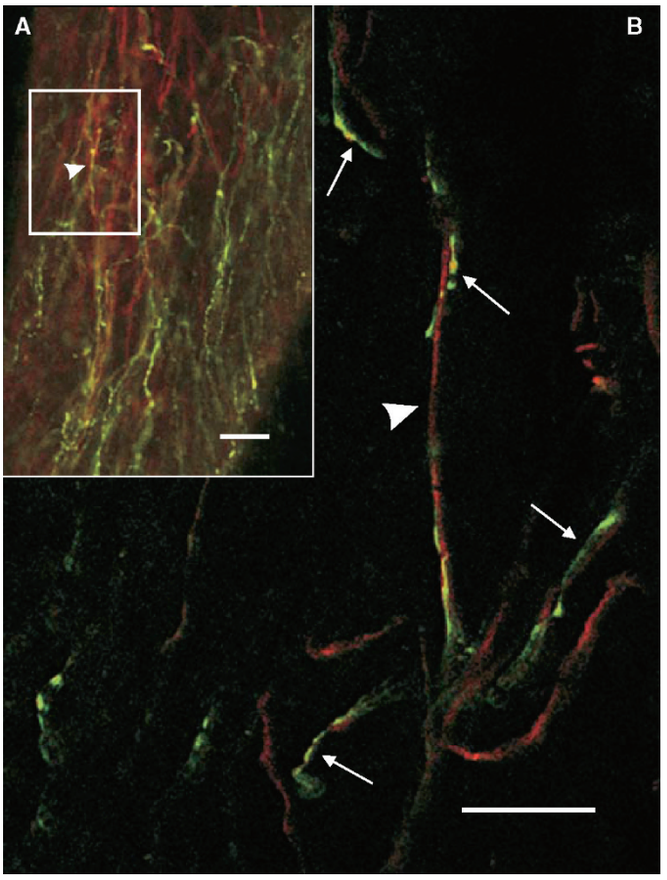

FIGURE 36.19. Colocalization. Nerve fibers labeled for peripherin (red) and CGRP (green) in tooth pulp from rats 3 weeks of age. Initial observations with a 20 × 0.75 NA Fluor lens (Nikon) (A) suggest a population of nerves co-immunostained for both proteins, appearing yellow. A 60 × 1.4 NA PlanApo lens (Nikon) with zoom = 2 (B) reveals two distinct populations of fibers: a thicker population labeled with peripherin (*arrowhead*), and smaller, beaded fibers, labeled with CGRP (*small arrows*). Both images are single planes from *z*-stacks. High magnification images were undersampled 60% laterally (150 nm vs. 83 nm) for this sample. Image (B) has been deconvolved by a maximum likelihood estimate algorithm (MLE). Scale bars represent 25 µm (A) and 10 µm (B).

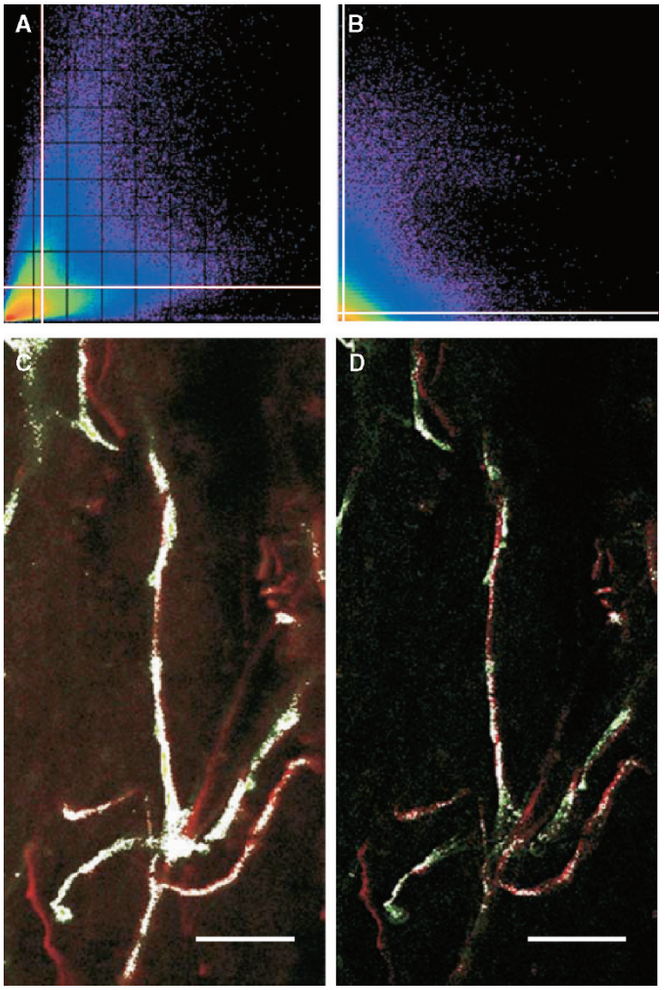

FIGURE 36.20. Fluorogram analysis of colocalization. 2D histograms of the volumes shown in Figure 36.19. Green intensities are plotted on the *y*-axis (0–255), and red intensities are plotted on the *x*-axis (0–255). The fluorogram before deconvolution (A) shows low intensity background in the green channel indicated by a layer of points lying above the *x*-axis and two correlations of unequal intensity possibly existing between the two channels. After restorative deconvolution the 2D histogram (B) has less background and shows the effect of background removal on putative colocalization. While (A) suggests a possible weak correlation in a bimodal distribution, (B) suggests a lack of colocalization. The white lines in both plots represent threshold levels applied to both channels for subsequent analysis on the volume (Table 36.3), and shown by white masks in panel (C) and (D). Panel (C) is the same field as that shown in Figure 36.19(B), but taken from the volume before deconvolution, and panel (D) is the same field after deconvolution. The scale bar represents 10 µm.

tion shows that the two labels may be co-existing (as noted by yellow) only where the fibers cross, or in some of the thickened regions along the small green fibers. Given that the *z*-resolution of the confocal microscope is significantly less than the *xy*-resolution, such overlaps may simply be due to the diminished *z*-resolution.

The 2D histograms in Figure 36.20 are derived from the high-resolution volume shown in Figure 36.19(B), and graphically demonstrate the impact on colocalization of background removal through deconvolution. The 2D histogram of the original (non-deconvolved) volume [Fig. 36.20(A)] displays two putative correlations, suggesting that each fiber is predominantly labeled for one protein, but containing the other protein in reduced amount. Pixels plotting close to the *x*-axis represent low intensity green label, such as the line of pixels very close to the *x*-axis (below the threshold line) indicating low-intensity background fluorescence in the green channel that associates with all levels of red fluorescence. Pixels plotting near the *y*-axis represent low intensity red label.

The 2D histogram changes dramatically after restorative deconvolution by maximum likelihood estimation (MLE, using Huygens, Scientific Volume Imaging) of the *z*-stack [Fig. 36.20(B)]. The low-intensity background from the green channel has been removed and the two regions of correlation observed in Figure 36.20(A) have been sharply reduced, suggesting that they were due to blur, as does the fact that most pixels are now shifted towards the *x*- or *y*-axis.

The impact of MLE on the correlation coefficients is shown in Table 36.3. The red and green labels show very high correlations in the original, undeconvolved low resolution volume [Fig. 36.19(A)], with values of 0.817 and 0.896 for *R* and *r*, respectively, in Table 36.3, Line 1. The colocalization coefficients *M*1 and *M*2 indicate that all voxels are colocalized because 100% of voxels in each channel are contributing to the colocalization. The higher

TABLE 36.3. Effect of MLE and Threshold on Colocalization

	Sample	MLE	Threshold	*R*	*r*	*M*1	*M*2
1	Fig. 36.19(A)	No	No	0.817	0.896	1.00	1.00
2	Fig. 36.19(B)	No	No	0.624	0.803	1.00	1.00
3	Fig. 36.19(B)	No	37/37	0.457	0.461	0.496	0.789
4	Fig. 36.19(B)	Yes	No	0.345	0.475	0.807	0.833
5	Fig. 36.19(B)	Yes	20/20	0.298	0.303	0.254	0.556

resolution volume [Fig. 36.19(B)] displays some reduction in both Pearson's coefficient and overlap coefficient (Table 36.3, Line 2) as the two populations of fibers are now resolved into separate objects. However, the colocalization coefficients for both channels are still at unity suggesting either perfect correlation or, more likely, significant levels of background.

MLE processing also changes the colocalization values, as shown in Table 36.3, Line 4. The amount of correlation from Pearson's coefficient drops to 34.5% and the overlap coefficient is reduced to 47.5%. The proportion of contribution to colocalization by the two channels (*M*1 and *M*2) are reduced to 80.7% for the red channel (*M*1) and 83.3% for the green channel (*M*2).

The threshold is important for determining the level of fluorescence that is to be considered significant. Thresholds were set for both channels by measurements of presumed background from the darker regions between the labeled fibers. These thresholds are represented by the white lines in Figure 36.20(A), at a threshold of 37 for the original image stack and at a threshold of 20 in Figure 36.20(B), the fluorogram of the volume after MLE. Table 36.3 provides the corresponding coefficients for the volumes following application of thresholds. The field in Figure 36.20(C) is the same field as in Figure 36.19(B), but taken from the high resolution volume before deconvolution. The white mask represents the pixels above threshold, as applied to this image plane. Figure 36.19(D) is the same field as Figure 36.19(B), taken from the volume after deconvolution. Pixels above the threshold applied to this image after deconvolution are represented by the white mask. The differences between Figure 36.20(C) and Figure 36.20(D) not only include the difference in number of colocalized pixels, but extend to the apparent thicknesses of the nerve fibers and background around the fibers.

Clearly, the apparent colocalization in the low magnification image and the high-resolution image was due to blending of the two channels by blur, noise and bleed-through. Restorative deconvolution reduced these contributions in a far more meaningful manner than was possible with simple thresholding. The remaining colocalization in this example is likely due to bleed-through, blur at the intersections of fibers, as well as blur from fibers in adjacent volume planes (not shown).

Using deconvolution, direct inspection of the image, and the 2D histogram in conjunction with the quantitative analysis tools available for colocalization can provide far greater insight into the relationships between the two labels in a volume than can any single tool alone. While we may be left with questions regarding the exact nature and extent of colocalization in this example, these tools can be used together to indicate directions that might be taken to determine the relationship between these two proteins more closely. Careful use of adequate controls to establish acquisition parameters that avoid bleed-through, noise, blur and autofluorescence, as described in detail by Costes *et al.* 2004, is essential for obtaining sound datasets for colocalization.

DISCUSSION

Recent advances spanning only the past 20 to 30 years have fueled extremely rapid development and popular adoption of laser-scanning microscopy as a practical and uniquely powerful tool for scientific discovery. The capabilities of these instruments have two faces — on one hand, they can gather light with unprecedented sensitivity, lack of noise, and resolution so that we can work at the limits of physics on biological questions that were unapproachable in an earlier era. On the other hand, they can also generate exquisitely stunning images of artifact or elevate the most mundane source of background into signals that overwhelm all meaningful information from the sample. Adequate controls are an absolute requirement to understand the interplay of the instrument controls and your samples. The regular application of standard confidence tests applied to both the instrument and the biological samples serve to demonstrate the outstanding capabilities of a well-maintained imaging system as well as providing meaningful information on the limitations of such equipment.

To ensure maximum productivity, it is advantageous to monitor the progress of declining performance so that the system may be restored to peak performance before the potential for grievous artifact or frank system failure becomes a reality. Murphy's Law dictates that there is a disproportionate chance such problems will be discovered at the onset of an important experiment or when results are needed in the face of looming deadlines. Quantitative measures of performance may serve to aid remote diagnosis by a field engineer and expedite subsequent ordering of the necessary parts. It is hoped that the tests outlined in this chapter will aid you in realizing the goals of data integrity, peak performance, and high instrument reliability when using laser-scanning confocal microscopes in a variety of environments.

ACKNOWLEDGMENTS

The images used to illustrate colocalization (Fig. 36.19 and Fig. 36.20) were generously provided by Dr. Orapin Veerayutthwilai (DDS, MS), Department of Oral Biology, and Dr. Margie Byers (PhD), Department of Anesthesiology, University of Washington, Seattle, WA. The image of a subresolution fluorescent bead in Figure 36.6 was kindly provided by Michael Weiss, Pacific Agri-Food Research Centre, Summerland, BC, Canada.

REFERENCES

Agnati, L.F., Fuxe, K., Torvinen, M., Genedani, S., Franco, R., Watson, S., Nussdorfer, G.G., Leo, G., Guidolin, D., 2005, New methods to evaluate colocalization of fluorophores in immunocytochemical preparations as exemplified by a study on A_{2A} and D_2 receptors in Chinese hamster ovary cells, *J. Histochem. Cytochem.* 53:941–953.

Akinyemi, O., Boyde, A., Browne, M.A., Hadravsky, M., and Petran, M., 1992, Chromatism and confocality in confocal microscopes, *Scanning* 14:136–143.

Booth, M.J., and Wilson, T., 2001, Refractive-index-mismatch induced aberrations in single-photon and two-photon microscopy and the use of aberration correction, *J. Biomed. Opt.* 6:266–272.

Brakenhoff, G.J. Wurpel, G.W.H., Jalink, K., Oomen, L., Brocks, L., and Zwier, J.M., 2005, Characterization of sectioning fluorescence microscopy with thin uniform fluorescent layers: Sectioned imaging property or SIPcharts. *J. Microsc.* 219:122–132.

Browne, M.A., Akinyemi, O., and Boyde, A., 1992, Confocal surface profiling utilizing chromatic aberration, *Scanning* 14:145–153.

Carlsson, K., 1991, The influence of specimen refractive index, detector signal integration, and non-uniform scan speed on the imaging properties in confocal microscopy, *J. Microsc.* 163:167–178.

Costes, S.V., Daelemans, D., Cho, E.H., Dobbin, Z., and Pavlakis, G., 2004, Automatic and quantitative measurement of protein-protein colocalization in live cells, *Biophys. J.* 86:3993–4003.

Cox, G., 1999, Measurement in the confocal microscope, *Methods Mol. Biol.* 122:357–371.

Cox, G., and Sheppard, C.J.R., 2004, Practical limits of resolution in confocal and nonlinear microscopy, *Microsc. Res. Tech.* 63:18–22.

Demandolx, D., and Davoust, J., 1995, Multicolor analysis in confocal immunofluorescence microscopy, *J. Trace Microprobe Tech.* 13:217–225.

Demandolx, D., and Davoust, J., 1997, Multicolour analysis and local image correlation in confocal microscopy, *J. Microsc.* 185:21–36.

Dickinson, M.E., Bearman, G., Tille, S., Lansford, R., and Fraser, S.E., 2001, Multi-spectral imaging and linear unmixing add a whole new dimension to laser scanning fluorescence microscopy, *Biotechniques* 31:1272–1278.

Garini, Y., Gil, A., Bar-Am, I., Cabib, D., and Katzir, N., 1999, Signal to noise analysis of multiple color fluorescence imaging microscopy, *Cytometry* 35:214–226.

Hibbs, A.R., 2004, *Confocal Microscopy for Biologists*, Kluwer Academic/Plenum Publishers, New York.

Hiraoka, Y., Sedat, J.W., and Agard, D.A., 1990, Determination of three-dimensional imaging properties of a light microscope system, *Biophys. J.* 57:325–333.

Ho, R., and Shao, Z., 1991, Axial resolution of confocal microscopes revisited. *Optik* 88:147–154.

Huth, U., Wieschollck., A, Garini, Y., Schubert, R., and Peschka-Süss, R., 2004, Fourier transformed spectral bio-imaging for studying the intracellular fate of liposomes, *Cytometry* 57A:10–21.

Hutter, H., 2004, Five-colour in vivo imaging of neurons in *Caenorhabditis elegans*, *J. Microsc*. 215:213–218.

LaMorte, V.J., Zoumi, A., and Tromberg, B.J., 2003, Spectroscopic approach for monitoring two-photon excited fluorescence resonance energy transfer from homodimers at the subcellular level, *J. Biomed. Opt.* 8:357–361.

Landmann, L., Deconvolution improves colocalization analysis of multiple fluorochromes in 3D data sets more than filtering techniques, 2002, *J. Microsc.* 208:134–147.

Landmann, L., and Marbet, P., 2004, Colocalization analysis yields superior results after image restoration, *Microsc. Res. Tech.* 64:103–112.

Lansford, R., Bearman, G., and Fraser, S.E., 2001, Resolution of multiple green fluorescent protein color variants and dyes using two-photon microscopy and imaging spectroscopy, *J. Biomed. Opt*. 6:311–318.

Maly, M., and Boyde, A., 1994, Real-time stereoscopic confocal reflection confocal microscopy using objective lenses with linear longitudinal chromatic dispersion, *Scanning* 16:187–193.

Manders, E.M.M., Stap, J., Brakenhoff, G.J., van Driel, R., and Aten, J.A., 1992, Dynamics of three-dimensional replication patterns during the S-phase, analysed by double labeling of DNA and confocal microscopy, *J. Cell Sci*. 103:857–862.

Manders, E.M.M., Verbeek, F.J., and Aten, J.A., 1993, Measurement of co-localization of objects in dual-colour confocal images, *J. Microsc*. 169:375–382.

Model, M., and Burkhardt, J., 2001, A standard for calibration and shading correction of a fluorescence microscope, *Cytometry* 44:309–316.

Neher, R., and Neher, E., 2004, Optimizing imaging parameters for the separation of multiple labels in a fluorescence image, *J. Microsc*. 213: 46–62.

Pawley, J.B., 1994, Sources of noise in three-dimensional microscopical data sets, In: *Three-Dimensional Confocal Microscopy: Volume Investigation of Biological Specimens* (J.K. Stevens, L.R. Mills, and J.E. Trogadis, eds.), Academic Press, London, pp. 47–93.

Pawley, J.B., 2000, The 39 steps: A cautionary tale of quantitative 3-D fluorescence microscopy, *Biotechniques* 28:884–886, 888.

Pawley, J.B., 2002, Limitations on optical sectioning in live-cell confocal microscopy, *Scanning* 24:241–246.

Scalettar, B.A., Swedlow, J.R., Sedat, J.W., and Agard, D.A., 1996, Dispersion, aberration and deconvolution in multi-wavelength fluorescence images, *J. Microsc*. 182:50–60.

Shaw, P.J., and Rawlins, D.J., 1991, The point-spread function of a confocal microscope: Its measurement and use in deconvolution of 3-D data, *J. Microsc.* 163:151–165.

Smallcombe, A., 2001, Multicolor imaging: The important question of co-localization, *Biotechniques* 30:1240–1246.

Stark, P.R.H., Rinko, L.J., and Larson, D.N., 2003, Fluorescent resolution target for super-resolution microscopy, *J. Microsc*. 212:307–310.

Tran, P., 2005, CCD cameras for fluorescence imaging of living cells, In: *Live Cell Imaging: A Laboratory Manual* (R.D. Goldman and D.L. Spector, eds.), Cold Spring Harbor Laboratory Press, Cold Spring Harbor, New York, pp. 87–100.

van den Doel, L.R., Klein, A.D., Ellenberger, S.L., Netten, H., Boddeke, F.R., van Vliet, L.J., and Young, I.T., 1998, Quantititative evaluation of light microscopes based on image processing techniques, *Bioimaging* 6:138–149.

van der Voort, H.T.M, Brakenhoff, G.J., and Janssen, G.C.A.M., 1988, Determination of the 3-dimensional optical properties of a confocal scanning laser microscope, *Optik* 78:48–53.

Van Steensel, B., van Binnendijk, E.P., Hornsby, C.D., van der Voort, H.T.M., Krozowski, Z.S., de Kloet, E.R., and van Driel, R., 1996, Partial colocalization of glucocorticoid and mineralocorticoid receptors in discrete compartments in nuclei of rat hippocampus neurons, *J. Cell Sci.* 109: 787–792.

Visser, T.D., Brakenhoff, G.J., and Groen, F.C.A., 1991, The one-point fluorescence response in confocal microscopy, *Optik* 87:39–40.

Wallace, W., Schaefer, L.H., and Swedlow, J.R., 2001, A workingperson's guide to deconvolution in light microscopy, *Biotechniques* 31:1076–1097.

Wilson, T., and Juskaitis, R., 1995, The axial response of confocal microscopes with high numerical aperture objective lenses, *Bioimaging* 3:35–38.

Young, M., 2000, Impulse response and transfer function, In: *Optics and Lasers* (M. Young, ed.), Springer-Verlag, New York, pp. 181–192.

Zucker, R.M., and Lerner, J.M., 2004, Calibration and validation of confocal spectral imaging systems, *Cytometry* 62A:8–34.

Zucker, R.M., and Price, O.T., 1999, Practical confocal microscopy and the evaluation of system performance, *Methods* 18:447–458.

Zucker, R.M., and Price, O.T., 2001a, Evaluation of confocal microscopy system performance, *Cytometry* 44:273–294.

Zucker, R.M., and Price, O.T., 2001b, Statistical evaluation of confocal microscopy images, *Cytometry* 44:295–308.

Zwier, J.M., Van Rooij, G.J., Hofstraat, J.W., and Brakenhoff, G.J., 2004, Image calibration in fluorescence microscopy, *J. Microsc.* 216:15–24.